Mesh generation for periodic 3D microstructure models and computation of effective properties

revised manuscript

Manuel Landstorfer[1,**], Benedikt Prifling[2] , Volker Schmidt[2]

[1] Weierstrass Institute for Applied Analysis and Stochastics (WIAS), 10117 Berlin, Germany

[2] Institute of Stochastics, Ulm University, 89069 Ulm, Germany

November 25, 2020

Abstract

Understanding and optimizing effective properties of porous functional materials, such as permeability or conductivity, is one of the main goals of materials science research with numerous applications. For this purpose, understanding the underlying 3D microstructure is crucial since it is well known that the materials' morphology has a significant impact on their effective properties. Because tomographic imaging is expensive in time and costs, stochastic microstructure modeling is a valuable tool for virtual materials testing, where a large number of realistic 3D microstructures can be generated and used as geometry input for spatially-resolved numerical simulations. Since the vast majority of numerical simulations is based on solving differential equations, it is essential to have fast and robust methods for generating high-quality volume meshes for the geometrically complex microstructure domains. The present paper introduces a novel method for generating volume-meshes with periodic boundary conditions based on an analytical representation of the 3D microstructure using spherical harmonics. Due to its generality, the present method is applicable to many scientific areas. In particular, we

---

*Corresponding author: Manuel.Landstorfer@wias-berlin.de

1

present some numerical examples with applications to battery research by making use of an already existing stochastic 3D microstructure model that has been calibrated to eight differently compacted cathodes.

1 Introduction

Porous media can be found in many natural as well as artificial physical, biological and chemical systems. From the composition of soils [1, 2], through which liquids seep into the ground water, to the mechanical stiffness of cements [3, 4], from battery electrodes [5, 6, 7], in which lithium ions are stored, to sponge-based filtration materials [8]: the porous microstructure of the respective system has a crucial impact on the overall behavior [9]. For example, the morphology of electrodes in lithium-ion batteries significantly influences the electrochemical properties [10, 11, 12, 13], which is the main reason why tailored structuring and manufacturing of anodes and cathodes is one promising approach to improve the performance of the cell [14, 15, 16]. Thus, it is a major issue in many research areas to design the microstructure in such a way that the overall performance, e.g. permeability, electrical conductivity, mechanical stiffness, energy density and further quantities, is optimized.

1.1 Mathematical background

From a mathematical point of view, the impact of the 3D morphology of porous media on their macroscopic behavior, e.g., the flow rate of water through soil or the flux of lithium ions through a battery electrode, can be studied with homogenization techniques. A prominent and mathematically sound tool is periodic homogenization theory [17], which assumes that the porous medium, given as a certain domain Ω, is a periodic repetition of some representative volume element ω, see Fig. 1. This method allows to derive a set of partial differential equations (PDEs) for which the porous microstructure is not spatially resolved anymore. This significantly reduces the numerical complexity of the problem. The method is based on an asymptotic expansion of the balance equation in terms of ε, which is the ratio between a macro-scale length L and the cell-scale length ℓ, $i.e.$, $\varepsilon = \frac{\ell}{L}$. In the asymptotic limit, where $\varepsilon \to 0$, a set of homogenized balance equations is then obtained, together with some porous media parameters.

Consider the decomposition $\Omega = \Omega_E \cup \Omega_S$, where the set Ω_E is simply connected and corresponds exemplarily to an electrolyte phase, and Ω_S is multiply connected, denoting exemplarily a solid phase. The interface between Ω_E and Ω_S is denoted by $\Sigma_{E,S}$. As already mentioned above, Ω is a periodic repetition of the unit cell

$\omega = \omega_{\text{E}} \cup \omega_S$, and the common interface $\sigma_{\text{E,S}} = \omega_{\text{E}} \cap \omega_S$.
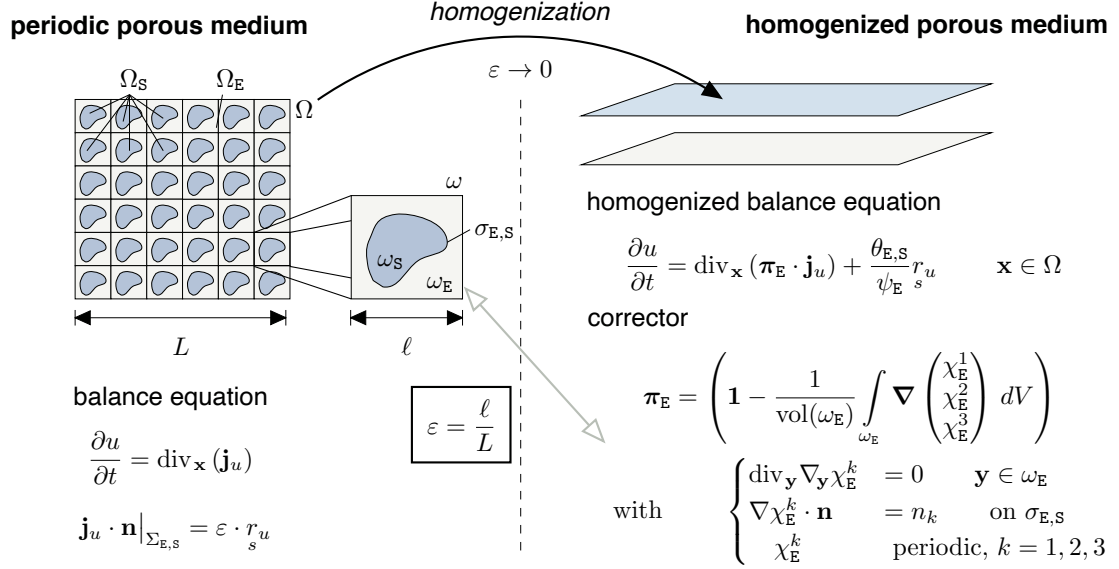

Figure 1: Sketch of a periodic porous medium in which a balance equation has to be solved (left). Homogenized porous medium subject to the homogenized balance equation (right).

For a scalar balance equation with surface reactions, we have the general model

$$\textbf{PDE1}: \quad \begin{cases} \frac{\partial u}{\partial t} = \text{div}_{\mathbf{x}}\left(\mathbf{j}_u\right) & \text{for all } \mathbf{x} \in \Omega_{\text{E}} \,, \\ \mathbf{j}_u \cdot \mathbf{n} = \varepsilon \cdot \underset{s}{r_u} & \text{on } \Sigma_{\text{E,S}} \,. \end{cases}$$

This problem is formally solved via the introduction of a multi-scale expansion $u(\mathbf{x}, t) = u^0(\mathbf{x}, \mathbf{y}, t) + \varepsilon \cdot u^1(\mathbf{x}, \mathbf{y}, t) + \mathcal{O}(\varepsilon^2)$, where $\mathbf{y} = \frac{\mathbf{x}}{\varepsilon}$, which yields a sequence of PDEs to determine the unknown functions u^j in the orders ε^j of the scaling parameter ε. Briefly summarized, with periodic homogenization [18, 17, 19] one obtains the following statements:

Order ε^0 yields essentially $u^0(\mathbf{x}, \mathbf{y}, t) = u^0(\mathbf{x}, t)$, i.e. , the leading order function u^0 is independent of the micro-scale $\mathbf{y}$.

Order ε^1 yields $u^1(\mathbf{x}, \mathbf{y}, t) = (\chi_{\text{E}}^1, \chi_{\text{E}}^2, \chi_{\text{E}}^3)^T \cdot \nabla_{\mathbf{x}} u^0$ as well as the condition

$$\textbf{CP1}: \quad \begin{cases} \text{div}_{\mathbf{y}} \nabla_{\mathbf{y}} \chi_{\text{E}}^k = 0 & \text{for all } \mathbf{y} \in \omega_{\text{E}}, \\ \nabla \chi_{\text{E}}^k \cdot \mathbf{n} = n_k & \text{on } \sigma_{\text{E,S}}, \\ \chi_{\text{E}}^k & \text{periodic} \,, \end{cases}$$

for the (geometrical) corrector function $\vec{\chi}_{\text{E}}$. The typeface $\vec{\chi}_{\text{E}} = \vec{\chi}_{\text{E}}(\mathbf{y})$ emphasizes that $\vec{\chi}_{\text{E}}$ is a (numerical) solution of the cell problem **CP 1**, which depends thus only on the micro-scale $\mathbf{y}$. Since u^0 and thus also $\nabla_{\mathbf{x}} u^0$ depend only on the macro-scale $\mathbf{x}$, *i.e.* $\nabla_{\mathbf{x}} u^0 := \vec{h}(\mathbf{x})$, the result $u^1 = \vec{\chi}_{\text{E}}(\mathbf{y}) \cdot \vec{h}(\mathbf{x})$ for the first successive term u^1 is a separation between microscopic geometrical effects and macroscopic gradients of the leading order term $u^0(\mathbf{x})$. This is a central feature of (periodic) homogenization theory and we show in Section 4 how χ_{E} is related to the tortuosity of a microstructure.

Order ε^2 yields the PDE

$$\psi_{\text{E}} \frac{\partial u^0}{\partial t} = \text{div}_{\mathbf{x}} \left(\psi_{\text{E}} \boldsymbol{\pi}_{\text{E}} \cdot \mathbf{j}_u^0 \right) + a_{\text{E,S}} r_{u_s} \qquad \text{for all } \mathbf{x} \in \Omega \tag{1}$$

for the leading order term u^0 and the leading order flux $\mathbf{j}_u^0$, where the porous media parameters are given by

1. the porosity (or phase fraction) of Ω_{E},

$$\psi_{\text{E}} = \frac{1}{\text{vol}(\omega)} \int_{\omega_{\text{E}}} 1 dV \ ,$$

2. the interfacial area of $\Sigma_{\text{E,S}}$,

$$a_{\text{E,S}} = \frac{1}{\text{vol}(\omega)} \int_{\sigma_{\text{E,S}}} 1 dA \ ,$$

3. and the (flux) corrector,

$$\boldsymbol{\pi}_{\text{E}} = \left(\mathbf{1} - \frac{1}{\text{vol}(\omega_{\text{E}})} \int_{\omega_{\text{E}}} \boldsymbol{\nabla} \begin{pmatrix} \chi_{\text{E}}^1 \\ \chi_{\text{E}}^2 \\ \chi_{\text{E}}^3 \end{pmatrix} dV \right) \ . \tag{2}$$

After the homogenization procedure the index ^{0} of the leading order term is typically dropped and considered as *the* macroscale variable. If $\mathbf{j}_u$ is a diffusion or heat flux, *e.g.*, $\mathbf{j}_u = D_u \cdot \nabla u$, the corrector $\boldsymbol{\pi}_{\text{E}}$ yields the effective diffusion coefficient (or conductivity) $D_{\text{E}}^{\text{eff}} = \boldsymbol{\pi}_{\text{E}} \cdot D_u$. The corrector $\boldsymbol{\pi}_{\text{E}}$ is thus also related to the *tortuosity* of the porous medium.

For the Stokes problem in a similar manner we obtain

$$\textbf{PDE2}: \quad \begin{cases} \nabla p - \varepsilon^2 \mu \mathrm{div}\nabla\mathbf{v} = \mathbf{f} & \text{for all } \mathbf{x} \in \Omega_{\mathrm{E}}, \\ \mathrm{div}\,\mathbf{v} = 0 & \text{for all } \mathbf{x} \in \Omega_{\mathrm{E}}, \\ \mathbf{v} = 0 & \text{on } \Sigma_{\mathrm{E,S}}, \end{cases}$$

where periodic homogenization leads to the Darcy flow

$$\mathbf{v} = \frac{1}{\mu}\kappa_{\mathrm{E}}(\mathbf{f} - \nabla p) \qquad \text{for all } \mathbf{x} \in \Omega_{\mathrm{E}}^{\mathrm{Hom}},$$

$$\mathrm{div}\,\mathbf{v} = 0 \qquad\qquad \text{for all } \mathbf{x} \in \Omega_{\mathrm{E}},$$

$$\mathbf{v} \cdot \mathbf{n}\big|_{\partial\Omega_{\mathrm{E}}^{\mathrm{Hom}}} = 0 \ .$$

The corrector κ_{E} is frequently called a permeability tensor, where

$$(\kappa_{\mathrm{E}})_{j,k} = \frac{1}{\mathrm{vol}(\omega_{\mathrm{E}})} \int\limits_{\omega_{\mathrm{E}}} \nabla\mathbf{w}_j \cdot \nabla\mathbf{w}_k \, dV,$$

and determined from the cell problem [20]

$$\textbf{CP2}: \quad \begin{cases} \nabla_{\mathbf{y}} q_k - \mathrm{div}_{\mathbf{y}}\nabla_{\mathbf{y}}\mathbf{w}_k = \mathbf{e}_k & \text{for all } \mathbf{y} \in \omega_{\mathrm{E}}, \\ \mathrm{div}\,\mathbf{w}_k = 0, \\ \mathbf{w}_k = 0 \quad \text{on } \sigma_{\mathrm{E,S}}, \\ \quad q_k, \mathbf{w}_k \quad \text{periodic, } k = 1, 2, 3. \end{cases}$$

1.2 Basic idea of mesh generation

For every PDE problem, *e.g.*, PDE1 or PDE2 described above, periodic homogenization leads to a different cell problem, *i.e.*, CP1 or CP2, which has to be solved in order to determine the effective porous media parameters. However, all of these cell problems do have in common that some stationary PDE system has to be solved on the periodic representative volume element ω. Since this is analytically possible only for a very tiny amount of geometries, the cell problems have in general to be solved numerically. And, in order to so, adequate discretizations of ω are required.

Various approaches for the discretization of the representative volume element ω exist and we briefly review exclusively those which ensure the periodicity of ω. The most simple approach is a voxel based discretization of ω, with equal edge length of the voxel in all three dimensions. This *format* of discretization is widely used in 3D imaging. However for the purpose of numerical calculations voxel based meshes are inappropriate, (i) because the computational degrees of freedom scale

with $\mathcal{O}(N)^3$ for N equally sized voxels [3], or (ii) because local refinements (or coarsening), leading to $\mathcal{O}(N)^{3-\alpha}, \alpha > 0$, lead to hanging nodes[1], which are numerically very problematic. To get rid of these problems a mesh for numerical calculations in 3D is typically built by tetrahedra, with which a 3D geometry can be discretized and locally refined without producing hanging nodes. This yields far more efficient numerical calculations and the corresponding meshes are said to be of *high quality*. Numerical simulations of 3D microstructures allow then for a virtual materials testing [21, 22].
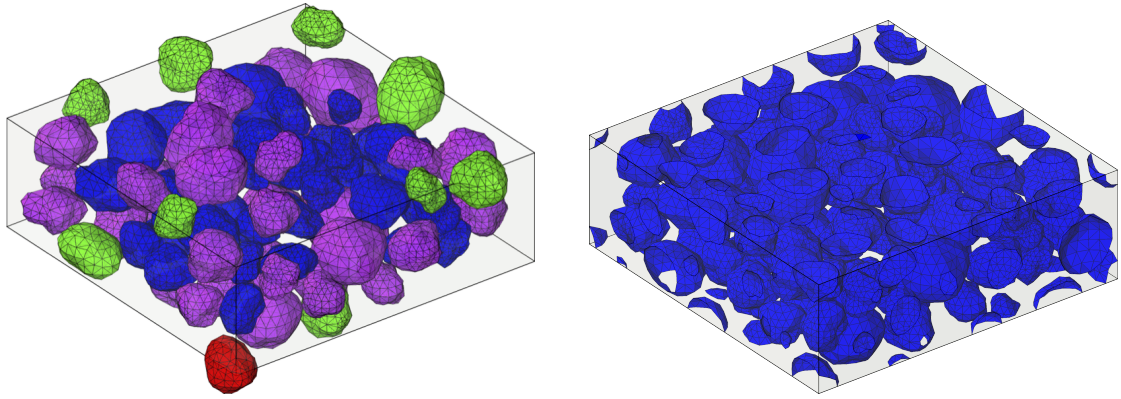
The generation of volumetric meshes for realistic microstructures is an interdisciplinary topic and various approaches are found throughout the literature [23, 24, 25]. A central aspect is the assumption regarding the geometrical shape of the particles or inclusions in the microstructure. For example a rather general approach of modeling inclusions in matrix materials assumes ellipsoidal shapes [26], which is explicitly exploited in the periodic mesh generation. However, tomographic imaging methods have shown that realistic 3D microstructures of various functional materials are significantly more complex. A flexible tool to model and simulate the morphology of such particle systems is hence desirable and we propose a complete pipeline for this issue.

1.3 Outline

In this paper, we propose a robust mesh generation for periodic representative volume elements of realistic microstructures, see Fig. 2, with geometrically more flexible star-shaped particles.

---

[1]A hanging node is a node of a mesh

(a) Colors encode the number of inter-sections with the periodicity box: 0 (blue), 1 (magenta), 2 (green), 3 (red).

(b) Intersection free surface mesh, with periodic repetitions of the particle segments intersecting the periodicity box.

Figure 2: Cutout of a porous battery electrode, consisting of several active particles, and the periodicity box.

The method is based on a description of the microstructure in terms of spherical harmonics, a subsequent surface mesh generation of $\partial\omega_\mathrm{E}$ and $\partial\omega_\mathrm{S}$, and finally a volume mesh generation based on TetGen [27]. The proposed method can be applied to a broad spectrum of scenarios arising in different fields of research since numerous scientific problems involve solving a system of differential equations on periodic porous media. Another advantage of the presented approach is that periodic boundary conditions can be easily applied in x-, y- and z-direction as well as to an arbitrary subset of directions. This can be used for example in battery research, where the size of electrodes is typically several orders of magnitudes larger in in-plane direction compared to the thickness of the electrode such that it is reasonable to consider periodic boundary conditions in two directions.

The rest of this paper is organized as follows. In Section 2, we describe the generation of periodic 3D microstructures based on spherical harmonics and a stochastic microstructure model. Then, in Section 3, the generation of a quality volume mesh on the basis of the representation of the particle system via spherical harmonics is explained. In Section 4, some numerical examples are presented. Finally, in Section 5, the paper is concluded by a summary of the main results and an outlook to possible future research is given.

2 Generation of periodic porous 3D microstructures

To generate a periodic representative volume element ω, we use the stochastic microstructure modeling approach described in [21], which basically consists of three
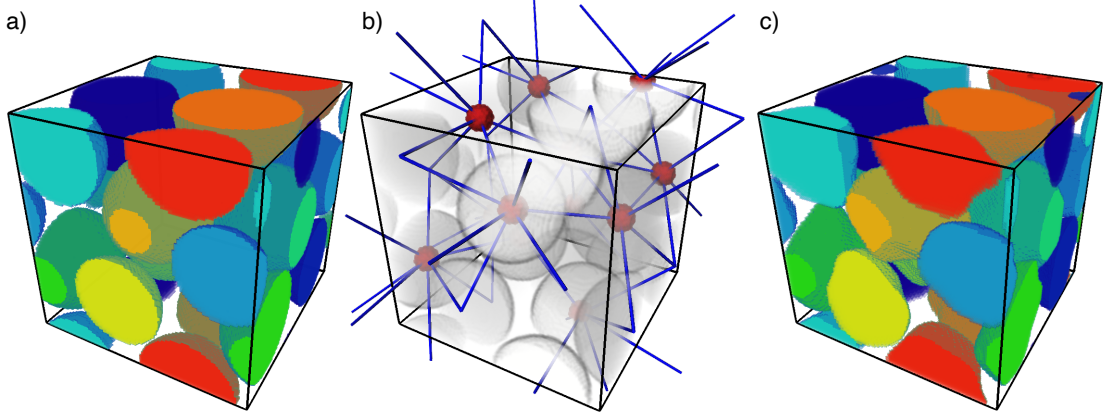
Figure 3: a) Generation of a non-overlapping sphere packing, see Section 2.1. b) Construction of the periodic connectivity graph (red: sphere, blue: connection of two spheres). c) Subsequent modeling of non-spherical particles via spherical harmonics accounting for the connectivity graph.

steps. First, a non-overlapping sphere packing is generated, where the volume fraction of the solid phase $\psi_{\mathrm{S}} = 1 - \psi_{\mathrm{E}}$ as well as the particle size distribution $\mathcal{R}$ can be preset. More precisely, the radii of spheres are drawn from the predefined particle size distribution $\mathcal{R}$ until the target volume fraction is achieved. Initially, the midpoints of the spheres are chosen uniformly on the sampling window $W \subset \mathbb{R}^3$, which typically leads to a system of overlapping spheres. In order to obtain a non-overlapping sphere packing, a rearrangement algorithm is used, which will be described in detail in Section 2.1. Each sphere acts as a placeholder and models the location as well as the size of a non-spherical particle, which will finally replace the underlying sphere. The second step is the construction of a connectivity graph $G = (V, E)$, where V is the (random) set of sphere midpoints obtained in the first step. If there is an edge $e = (v_1, v_2)$ between two vertices $v_1, v_2 \in V$, then the corresponding particles are forced to touch each other. Finally, in the third step, each sphere is replaced by a non-spherical particle generated via spherical harmonics, which fulfils the requirements of the connectivity graph. This modeling approach described in [21] is visualized in Figure 3, where periodic boundary conditions are taken into account. The representation of particles based on spherical harmonics will be discussed in detail in Section 2.2.

2.1 Force-biased sphere packing algorithm

As already mentioned above, a rearrangement algorithm will be used in order to completely remove the overlap between the spheres. For this purpose, the

8

algorithm considered in [28] is used, which is based on the force-biased algorithm for equally sized spheres [29]. For convenience, the basic idea of this force-biased algorithm will be explained shortly at this point. Given a set of radii $r_1, ..., r_N > 0$ and the initial midpoints $\mathbf{x}_1^{(0)}, ..., \mathbf{x}_N^{(0)}$, we additionally consider an inner radius $r_{\texttt{in}}$ and an outer radius $r_{\texttt{out}}$, which are changing during the execution of the iterative algorithm. The inner radius at time t is defined by $r_{\texttt{in}}^{(t)} = \min\left\{\frac{\|\mathbf{x}_i^{(t)} - \mathbf{x}_j^{(t)}\|}{r_i + r_j} : i, j = 1, ..., N, i \neq j\right\}$, where $\|\mathbf{x}\|$ denotes the Euclidean norm of $\mathbf{x}$. The collective rearrangement algorithm will terminate if $r_{\texttt{in}}^{(t)} \geq 1$, which implies that the sphere system is non-overlapping. The outer radius $r_{\texttt{out}}^{(t)}$ decreases over time, where a certain parameter τ controls the speed of shrinking. The following equation describes the rule for updating the midpoints of the spheres:

$$\mathbf{x}_i^{(t+1)} = \mathbf{x}_i^{(t)} + \frac{\rho}{r_i} \sum_{j=1, \, j \neq i}^{N} \rho_{ij} r_i r_j \left(4 \cdot \frac{\|\mathbf{x}_i^{(t)} - \mathbf{x}_j^{(t)}\|^2}{(r_i + r_j)^2} - (r_{\texttt{out}}^{(t)})^2\right) \frac{\mathbf{x}_i^{(t)} - \mathbf{x}_j^{(t)}}{\|\mathbf{x}_i^{(t)} - \mathbf{x}_j^{(t)}\|}$$

Since $\rho_{ij} = \mathbb{1}(B(x_i^{(t)}, r_{\texttt{out}}^{(t)} r_i) \cap B(x_j^{(t)}, r_{\texttt{out}}^{(t)} r_j) \neq \emptyset)$, where $\mathbb{1}(B)$ denotes the indicator of the set B, the force acting on the i-th sphere only depends on spheres in a certain local neighborhood around $\mathbf{x}_i^{(t)}$, which is essential for an efficient implementation of the algorithm. Furthermore, since it is crucial to obtain a periodic microstructure, we take periodic boundary conditions into account when computing the distance $\|\mathbf{x}_i^{(t)} - \mathbf{x}_j^{(t)}\|$. More precisely, for $\mathbf{x}_i^{(t)} = (x_{i,1}^{(t)}, x_{i,2}^{(t)}, x_{i,3}^{(t)}), \mathbf{x}_j^{(t)} = (x_{j,1}^{(t)}, x_{j,2}^{(t)}, x_{j,3}^{(t)}) \in \mathbb{R}^3$ it holds that

$$\|\mathbf{x}_i^{(t)} - \mathbf{x}_j^{(t)}\| = \sqrt{\sum_{k=1}^{3} \min\left\{|x_{i,k}^{(t)} - x_{j,k}^{(t)}|, s_k - |x_{i,k}^{(t)} - x_{j,k}^{(t)}|\right\}^2}, \tag{3}$$

where $s_1, s_2, s_3 > 0$ denote the size of the observation window W in x-, y- and z-direction, respectively. In addition, the periodic boundary conditions have to be applied when the updated position $\mathbf{x}_i^{(t+1)}$ is no longer contained in the sampling window $W \subset \mathbb{R}^3$. Since the non-overlapping sphere system is periodic by definition, the final system of non-spherical particles fulfils periodic boundary conditions, too. However, this step also allows to implement periodic boundary conditions only with regard to certain directions. For this purpose, the summands of Eq. (3) are replaced by $|x_{i,k}^{(t)} - x_{j,k}^{(t)}|$ for those directions $k \in \{1, 2, 3\}$, for which no periodic boundary conditions are applied. A visualization of the working principle of this force-biased collective rearrangement algorithm can be found online as supplementary material. Finally, note that the sphere packing algorithm described above is only capable of generating packing densities up to approximately 65%, where for packing densities of more than 60%, a so-called core-shell ratio is used, see [21] for further details.

2.2 Representation of particles via spherical harmonics

In order to generate non-spherical particles, we make use of spherical harmonics [30], which are a frequently used mathematical tool in a variety of research areas, ranging from quantum mechanics [31] to heat transfer [32]. Assuming star-shaped particles, which is reasonable in a wide range of applications, one can analytically describe the shape of a single particle by its center $\mathbf{b} \in \mathbb{R}^3$ and the radius function $R : (0, 2\pi] \times (0, \pi] \to \mathbb{R}$ since the spherical harmonic functions $\{Y_\ell^m : [0, \pi] \times [0, 2\pi) \to [0, \infty) : \ell \in \mathbb{N}_0, m \leq \ell\}$ form a basis for the family of square integrable functions defined on the unit sphere $\mathbb{S} = \{x \in \mathbb{R}^3 \ : \ \|x\| = 1\}$, see [33]. More precisely, for any $(\theta, \varphi) \in (0, 2\pi] \times (0, \pi]$ it holds that

$$
\begin{aligned}
R(\theta, \varphi) = \sqrt{4\pi} \sum_{\ell=0}^{\infty} \sum_{m=-\ell}^{\ell} c_\ell^m Y_\ell^m(\theta, \varphi) &\approx \sqrt{4\pi} \sum_{\ell=0}^{L} \sum_{m=-\ell}^{\ell} c_\ell^m Y_\ell^m(\theta, \varphi) \\
= \sqrt{4\pi} \cdot \Big(\sum_{\ell=0}^{L} c_\ell^0 Y_\ell^0(\theta, \varphi) &+ 2 \cdot \sum_{m=1}^{\ell} \mathrm{Re}(c_\ell^m) \mathrm{Re}(Y_\ell^m(\theta, \varphi)) \\
&- \mathrm{Im}(c_\ell^m) \mathrm{Im}(Y_\ell^m(\theta, \varphi)) \Big),
\end{aligned}
$$

with coefficients $c_\ell^m \in \mathbb{C}$, spherical harmonic functions $Y_\ell^m : (0, 2\pi] \times (0, \pi] \to \mathbb{C}$ and the series expansion parameter $L \geq 0$. It is important to note that different definitions of spherical harmonics are used within different fields of research, where the most common source of confusion is the multiplicative factor $(-1)^m$, which is often called the Condon-Shortley phase, see [34]. Note that due to the multiplication of the double sum with $\sqrt{4\pi}$, a spherical particle with radius r is solely represented by the first coefficient $c_0^0 = r$. In addition, it is possible to estimate the complex coefficients c_ℓ^m from voxelized image data by the method described in [35] such that an analytical representation of non-spherical particles is obtained. The degree of smoothness can be controlled by the choice of the series expansion parameter L, see Figure 3 in [35]. Finally, a particle system consisting of N particles can thus be uniquely described by a list of centroids and the corresponding coefficients c_ℓ^m. In order to generate a system of non-spherical particles in a stochastic manner, Gaussian random fields on the sphere are used [36]. Note that each isotropic Gaussian random field $\{T(x), x \in \mathbb{S}\}$ exhibits the so-called Karhunen-Loève expansion

$$
T(x) \approx \sum_{\ell=0}^{L} C_\ell^0 Y_\ell^0(x) + 2 \cdot \sum_{m=1}^{\ell} \mathrm{Re}(C_\ell^m) \mathrm{Re}(Y_\ell^m(x)) - \mathrm{Im}(C_\ell^m) \mathrm{Im}(Y_\ell^m(x)),
$$

where we once again truncated the infinite sum by the parameter L. The complex random variables $\{C_\ell^m, \ell \in \{0, ..., L\}, m \leq \ell\}$ are independent and $\mathrm{Re}(C_\ell^m)$ as

10

well as $\mathrm{Im}(C_\ell^m)$ are normally distributed [37]. This finally allows for simulating non-spherical particles by drawing the coefficients c_ℓ^m from a multivariate normal distribution, see [38] for further technical details. Finally, the complex geometrical features of non-spherical particles can be described by the so-called angular power spectrum $A(1), ..., A(L) \geq 0$, which can be estimated from tomographic image data and used for simulating virtual but realistic particle systems, see e.g. [21, 38, 39]. This concludes the stochastic modeling of periodic 3D microstructures, where the analytical representation of the microstructure in terms of spherical harmonics is the basis for the construction of a quality volume mesh, as it is described in the next section.

3 Periodic mesh generation

We now discuss the mesh generation for the microstructures described in Section 2, yielding discrete approximations for ω and ω_{E}. Recall that the microstructure to be meshed has the representation $(\mathbf{x}_n^0, R_n)_n, n = 1, \dots, N$, where N is the number of particles. The surface of each particle $\mathbf{P}_n$ is parametrized by

$$\mathbf{x}_n = \mathbf{x}_n^0 + R_n(\theta, \varphi) \cdot \mathbf{e}_r\,, \quad \mathbf{e}_r = \begin{pmatrix} \sin\theta \cdot \cos\varphi \\ \sin\theta \cdot \sin\varphi \\ \cos\theta \end{pmatrix}\,, \quad \text{for } \theta \in (0, \pi], \varphi \in (0, 2\pi]\,, \quad (4)$$

with $\mathbf{x}_n^0$ being the midpoint and R_n the radius function of P_n. As explained in the previous section, R_n is expanded in terms of spherical harmonic functions, where the coefficients c_ℓ^m are deduced from a stochastic model described, e.g., in [21].

As a surface mesh $\mathbf{M}$ of a single particle, we consider a tupel $(\mathbf{v}, \mathbf{f})$ with $\mathbf{v} \in \mathbb{R}^{M_v \times 3}$ and $\mathbf{f} \in \mathbb{N}^{M_f \times 3}$, where M_v is the number of vertices (or node points) and M_f the number of faces of the mesh $\mathbf{M}$. A face $f_j = (f_{j1}, f_{j2}, f_{j3})$ is the j-th row of $\mathbf{f}$, defining a triangle $\mathbf{t}_j = (\mathbf{x}_{f_{j1}}, \mathbf{x}_{f_{j2}}, \mathbf{x}_{f_{j3}})$. A volume mesh $\mathbf{M}^V$ is a tupel $(\mathbf{v}, \mathbf{g})$ with $\mathbf{v} \in \mathbb{R}^{M_v \times 3}$ and $\mathbf{g} \in \mathbb{N}^{M_g \times 4}$. One entry of $\mathbf{g}$ describes a tetrahedron $g_j = (g_{j1}, g_{j2}, g_{j3}, g_{j4})$. Note that the boundary of a volume mesh is a (closed) surface mesh. In particular, a discrete approximation of particle $\mathbf{P}_n$, or, more precisely, a discrete approximation of its parametrized surface, is denoted by $\mathbf{M}_n = (\mathbf{v}_n, \mathbf{f}_n)$, with nodes $\mathbf{v}_n^i = \mathbf{x}_n(\theta_i, \varphi_i), i = 1, \dots, M_v$ and faces $\mathbf{f}_n$, where the definition of the angles $(\theta_i, \varphi_i) \in (0, 2\pi] \times (0, \pi]$ will be described later on in Section 3.1.

The microstructure is supposed to be periodic with respect to the bounding box $\mathbf{B} = \{B_k\}_{k=1,\dots,6}$, built by the (infinite) planes $B_1 = \{(x, y, z) \in \mathbb{R}^3 : x = x_{\min}\}$,

$B_2 = \{(x, y, z) \in \mathbb{R}^3 : y = y_{\min}\}$, and so forth, following the numbering of a classical 6-sided dice. The corresponding rectangle $\bar{B}_k$ is the plane B_k bounded by the other planes, $e.g.$, $\bar{B}_1 = \{(x, y, z) \in \mathbb{R}^3 : x = x_{\min}, y_{\min} \leq y \leq y_{\max}, z_{\min} \leq z \leq z_{\max}\}$.

We seek a volume mesh $\mathbf{M}_\omega^V$ of the unit cell ω, and, in particular, $\mathbf{M}_{\omega_{\mathrm{E}}}^V$ of the connected domain ω_{E}, which is achieved in the following steps:

1. Initial meshing of each particle $\mathbf{P}_n$,

2. Pairwise intersection of particles $(\mathbf{P}_n, \mathbf{P}_k)$ and local deformation to ensure non-intersection,

3. Intersection of particles $\mathbf{P}_n$ with the box $\mathbf{B} = \{B_k\}_k$, yielding intersection curves $\gamma_{n,k}$,

4. Meshing of the particles $\mathbf{P}_n$ and planes B_k subject to the intersection curves $\gamma_{n,k}$,

5. Building of a closed surface mesh $\mathbf{M}$ accounting for the periodic repetitions of all particles,

6. Construction of a quality volume $\mathbf{M}^V$ from the intersection free, closed surface mesh $\mathbf{M}$.

The workflow of the mesh generation is shown in Fig. 4. A central feature of the algorithm is a constrained Delaunay surface triangulation, which is achieved via appropriate rotations and stereographic projections. The algorithm has been implemented in Matlab and extensively tested at random microstructures, which were generated by the method explained in Section 2.
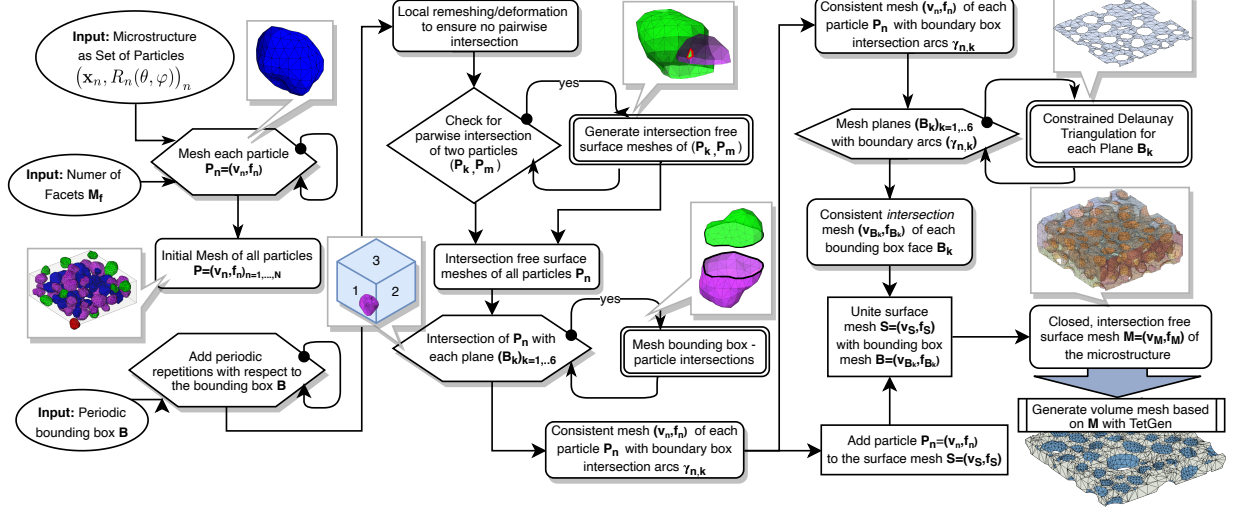
Figure 4: Workflow map of the mesh generation.

3.1 General methods

The following methods are frequently used in the mesh generation procedure proposed in this paper. Some methods of the `iso2mesh` toolbox [40] are frequently used during the surface mesh generation.

3.1.1 Meshing a single particle

Meshing a single particle $\mathbf{P}_n$ is essentially obtained in three steps, see also Fig.5:

1. Determine angles (θ_i, φ_i) such that the points $\mathbf{e}_r^i = \mathbf{e}_r(\theta_i, \varphi_i)$ are equidistributed on the unit sphere.

2. Compute the convex hull $\mathbf{f}$ of the meshpoints $(\mathbf{e}_r^i)_i$.

3. Compute the corresponding meshpoints on the particle surface given in Eq. (4) yielding the surface mesh $\mathbf{M}_n = (\mathbf{v}_n, \mathbf{f}_n)$ with $\mathbf{f}_n = \mathbf{f}$.

The equidistributed meshpoints on the unit sphere ensure that the triangles built by the convex hull operation are of almost equal size, shape and not degenerated (no agglomeration of meshpoints around the poles, no sharp or obtuse angles). Several methods exist to construct equidistributed meshpoints on a sphere, *e.g.*, via geodesic polyhedrons and their projections onto the unit sphere [41]. However, for a prescribed number M_v of meshpoints the method proposed by Deserno is rather convenient. It places points on the sphere such that that their distance in two orthogonal directions is locally always the same [42]. We use this method throughout

13

the present paper to compute the angle vectors $(\boldsymbol{\theta}, \boldsymbol{\varphi}) = \{(\theta_i, \varphi_i)\}_{i=1,\dots,M_v}$ for a prescribed number of meshpoints M_v. Note that the 3D microstructure, which is analytically described by spherical harmonic functions, can be represented as precisely as desired by increasing M_v, *i.e.*, there is no limitation by a certain resolution.
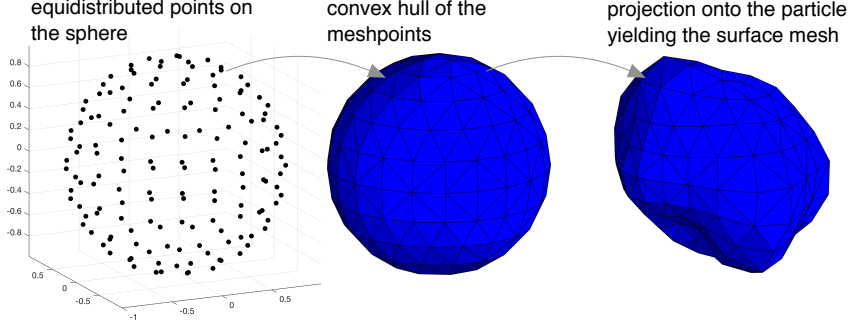

Figure 5: Mesh generation for a single particle based on the convex hull of a geodesic unit sphere.

The convex hull $\mathbf{f}$ of the equidistributed points on the sphere is computed with the *quickhull* algorithm proposed by Barber *et. al* [43], which is implemented in Matlab's `convhull` function [44]. We call the tupel $(\mathbf{x}, \mathbf{f})$ icosphere with M_v meshpoints and $M_f \approx 2 \cdot M_v$ facets.

Evaluating the spherical harmonics representation given in Eq. (4) for $(\boldsymbol{\theta}, \boldsymbol{\varphi})$ of the icosphere is straightforward by an explicit implementation of the first spherical harmonics functions $Y_{\ell,m}(\theta, \varphi), m = 0, .., \ell, \ \ell = 0, \dots, L$, where we put $L = 10$. This yields the initial surface mesh $\mathbf{M}_n = (\mathbf{v}_n, \mathbf{f}_n)$ with $\mathbf{f}_n = \mathbf{f}$ of each particle $\mathbf{P}_n, n = 1, \dots, N$.

3.1.2 General surface-surface intersections

To determine the intersection of two surface meshes $(\mathbf{M}_1, \mathbf{M}_2)$ we rely on an algorithm proposed by Möller [45] for fast triangle-triangle intersections and its Matlab implementation `Surface Intersection` provided by Tuszynski [46]. This method is widely used in computational geometry and determines the intersection points of two triangles in 3D in a robust and efficient manner. However, robustness issues can arise when triangles are nearly co-planar and a superior algorithm was recently proposed [47], which could in principle also be used within our pipeline. The method determines the N_I intersection points $\mathbf{v}_{1,2} \in \mathbb{R}^{N_I \times 3}$ of the intersecting facets as well as an edge graph $\mathbf{c}_{1,2} \in \mathbb{N}^{M_I \times 2}$ for the intersection points (see Fig. 6). The tupel $(\mathbf{v}_{1,2}, \mathbf{c}_{1,2})$ forms a discrete, oriented family of curves $\{\gamma_{1,2}^j\}_{j=1,\dots,N_j}$ with

$\gamma_{1,2}^{j} = (\mathbf{v}_{1,2}, \mathbf{c}_{1,2}^{j})$, where N_j is the number of arcs arising from the intersection, obtained by splitting the edge graph $\mathbf{c}_{1,2}$ accordingly.
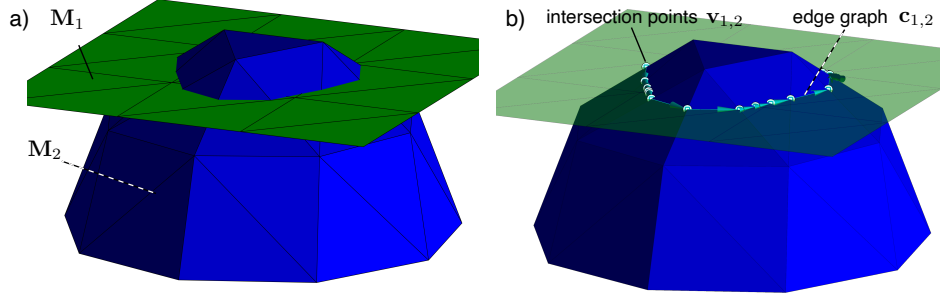

Figure 6: a) Intersection of two surface meshes $(\mathbf{M}_1, \mathbf{M}_2)$. b) Outcome of the triangle-triangle surface intersection: discrete curve $\gamma_{1,2} = (\mathbf{v}_{1,2}, \mathbf{c}_{1,2})$.

Note that the triangle-triangle intersections algorithm computes the intersection points on each arc of all intersecting triangles, resulting in a very fine boundary arc γ, *i.e.*, a discretization much finer than the average arc length of original mesh. This would result in far too finely resolved meshes near the intersection edge. To avoid this, we use a coarsening step on all arcs determined by `Surface Intersection`. We parametrize γ according to its arc length s by interpolating the arc points $\mathbf{v}_\gamma$ accordingly, yielding a curve function $\gamma = \gamma(s)$. Then we re-evaluate $\gamma(s)$ at equidistant arc length points s_i, yielding a proper discretization of the intersection curves.

3.1.3 Constrained Delaunay surface triangulations

A constrained Delaunay triangulation (CDT) is a special form of triangulation, where some conditions on the triangulation have to be fulfilled. Consider, for example, a (non-convex) polygon $\gamma = (\mathbf{v}_\gamma, \mathbf{c}_\gamma)$ and points $\mathbf{v}_{\text{in}}$ which lie inside the polygon. We seek a triangulation of $\mathbf{v} = (\mathbf{v}_\gamma, \mathbf{v}_{\text{in}})$ which ensures that the boundary of the triangulation is indeed γ. This can be achieved with constrained Delaunay triangulations [48, 49], where γ is prescribed as edge constraint. For 2D problems, *i.e.*, points in the plane bounded by a curve, this is rather straightforward and many implementations exist, where we mention, *e.g.*, the well-known Matlab implementation `delaunayTriangulation`.

However, for non-convex polygons on a 2D hyper-surface embedded in the 3D space the situation is much more complex. Here we seek a surface triangulation $\mathbf{M}$ of points on a surface bounded by a curve which lays on the surface. Note that this is very different from the "tetrahedralizations" of a 3D point cloud, forming

tetrahedra, bounded by a (closed) hyper-surface and resulting in a volume mesh $\mathbf{M}^V$. The problem arises when intersections between two particles or between a particle and the bounding box are considered. Since the particles are parametrized in terms of spherical harmonics, we can exploit this by conformal mappings from the sphere onto the plane.

A given arc $\gamma = (\mathbf{v}_\gamma, \mathbf{c}_\gamma)$ on the sphere forms a non-convex spherical polygon. Note that for a spherical triangle with the vertices $\mathbf{a}, \mathbf{b}, \mathbf{c}$ on the unit sphere, the area e and the centroid $\mathbf{d}$ can be computed as follows, see *e.g.* [50]:

$$e = \arccos\left(\mathbf{n_a}, \mathbf{n_b} + \arccos\left(\mathbf{n_b}, \mathbf{n_c}\right) + \arccos\left(\mathbf{n_c}, \mathbf{n_a}\right) - \pi \right.,$$

$$\mathbf{d} = \frac{1}{2se}\left(\mathbf{n_c}\arccos\left(\mathbf{a}, \mathbf{b}\right) + \mathbf{n_a}\arccos\left(\mathbf{b}, \mathbf{c}\right) + \mathbf{n_b}\arccos\left(\mathbf{c}, \mathbf{a}\right)\right) ,$$

where

$$\mathbf{n_c} = \frac{\mathbf{a} \times \mathbf{b}}{\|\mathbf{a} \times \mathbf{b}\|}, \quad \mathbf{n_a} = \frac{\mathbf{b} \times \mathbf{c}}{\|\mathbf{b} \times \mathbf{c}\|}, \quad \mathbf{n_b} = \frac{\mathbf{c} \times \mathbf{a}}{\|\mathbf{c} \times \mathbf{a}\|},$$

and $s = \text{sign}\langle\mathbf{a}, \mathbf{b} \times \mathbf{c}\rangle$ accounts for the orientation of the surface triangle, *i.e.*, an inner or outer triangle. Furthermore, consider a spherical polygon with vertices $\{\mathbf{v}_i\}_{i=1,\dots,N}$. Then, for each $i = 1, \dots, N-1$, let $\mathbf{d}_i$ denote the centroid of the spherical triangle with vertex set $\{\mathbf{v}_i, \mathbf{v}_{\bmod (i+1,N)}, \mathbf{v}_N\}$, e_i its area and s_i its sign. The spherical centroid $\bar{\mathbf{v}}$ is then given by

$$\bar{\mathbf{v}} = \frac{1}{2} \frac{\sum_{i=1}^{N-1} s_i e_i \mathbf{d}_i}{\sum_{i=1}^{N-1} s_i e_i} ,$$

and its projection onto the sphere by $\mathbf{n} = \frac{\bar{\mathbf{v}}}{\|\bar{\mathbf{v}}\|}$.
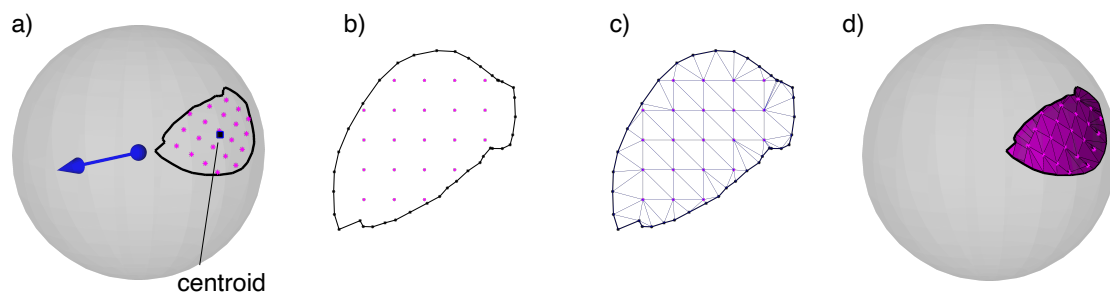

Figure 7: Spherical polygon and its centroid (a), stereographic projection (b), 2D constrained Delaunay triangulation (c), constrained surface mesh (d).

For a given arc $\gamma = (\mathbf{v}_\gamma, \mathbf{c}_\gamma)$ and interior points $\mathbf{v}_{\text{in}}$ we consider the following sequence of steps to generate a constrained surface mesh, see Fig. 7:

1. Compute the centroid $\bar{\mathbf{v}}$ of the spherical polygon γ and project it onto the sphere, resulting in a point $\mathbf{n}$ within[2] the spherical polygon.

2. Rotate the sphere such that $-\mathbf{n}$ becomes the north pole $(1, 0, 0)$.

3. Project the spherical polygon and its interior points onto the plane via the stereographic projection given by

$$u = \frac{x}{1-z} \quad \text{and} \quad v = \frac{y}{1-z}.$$

4. Perform a 2D constrained Delaunay triangulation in the (u, v)-plane resulting in a triangulation $\mathbf{f}$.

5. Consider $(\mathbf{v}, \mathbf{f})$ as constrained surface mesh $\mathbf{M}$.

We call this method "constrained surface Delaunay triangulation via stereographic projections". It will be extensively used in the following.

3.2 Generating quality volume meshes from surface meshes

3.2.1 Particle-particle intersections

In order to generate a volume mesh $\mathbf{M}^V$ from a surface mesh $\mathbf{M}$, it is of ultimate importance that $\mathbf{M}$ is intersection free. For two particles $\mathbf{P}_1$ and $\mathbf{P}_2$ this yields two possibilities: (i) an intersection and local re-meshing to form a unified, intersected particle, or (ii) a local deformation of $\mathbf{P}_1$ and $\mathbf{P}_2$ to ensure non-intersection. We decided for variant (ii) since it seems physically more meaningful, but switching to (i) is technically possible as well.

Based on the method described in Section 3.1.2, the intersection of two surface meshes $\mathbf{M}_1$ and $\mathbf{M}_2$ yields the intersection arcs $\gamma_{1,2}^j = (\mathbf{v}_{1,2}^j, \mathbf{c}_{1,2}^j)$. For each j we determine the normal plane approximating the 3D point cloud $\mathbf{v}_{1,2}^j$, yielding the corresponding normal vector $\mathbf{n}^j$. In the following, we drop the superscript j and determine the rotation matrix R such that $R \cdot \mathbf{n} = (1, 0, 0)$, where we rotate the particles accordingly. Next, the exterior mesh $\mathbf{f}_{i,o}, i = 1, 2$ of each particle is determined, which consists of all faces that do not intersect $\gamma_{1,2}$. However, the boundary of $\mathbf{f}_{i,o}$ is itself a closed, oriented curve, denoted by γ_i. We then translate

---

[2]In rare cases, simultaneous intersection with two planes can produce a strongly non-convex spherical polygon where the centroid is not inside. However, starting from the centroid, a point can be found nearby which is located on the intersection line of the two planes and additionally within the spherical polygon, which serves then as $\mathbf{n}$.

$\gamma_{1,2}$ by some distances d_1 and d_2 into $\mathbf{P}_1$ and $\mathbf{P}_2$, respectively, yielding the curves $\gamma_{1,2}^1$ and $\gamma_{1,2}^2$.
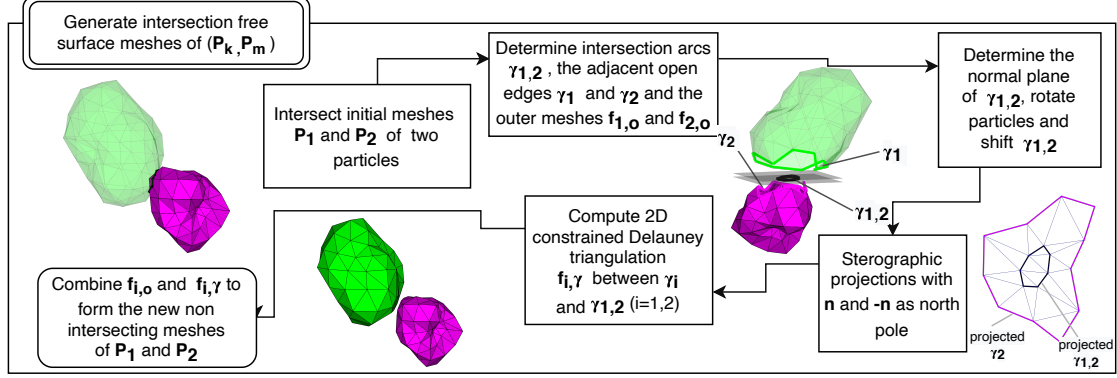

Figure 8: Detailed workflow map of the particle-particle intersection.

Then we use the method described in Section 3.1.3 to compute the surface constrained Delaunay triangulation of $\gamma_{1,2}^i$ bounded by the curve γ_i. This yields a triangulation $\mathbf{f}_{i,\gamma}$ of the former intersecting part of $\mathbf{P}_i$. Uniting $\mathbf{f}_{i,\gamma}$ with the unmodified exterior $\mathbf{f}_{i,o}$ yields a new surface triangulation $\mathbf{M}_i$ of particle $\mathbf{P}_i$, ensuring a non-intersection between $\mathbf{P}_1$ and $\mathbf{P}_2$. The workflow is shown in Fig. 8.

3.2.2 Intersections of particles with the bounding box

Next the particles are intersected with the bounding box $\mathbf{B}$. Recall that Fig. 2a shows an initial mesh of a microstructure and, color-coded, the number of intersections of each particle with the rectangles $\bar{B}_1, \ldots, \bar{B}_6$ forming the bounding box $\mathbf{B}$. Let $i_n \in \{0, 1, 2, 3\}$ denote the number of intersections of particle $\mathbf{P}_n$ with the rectangles $\bar{B}_1, \ldots, \bar{B}_6$. The number k_n of periodic repetitions of $\mathbf{P}_n$ (including the particle $\mathbf{P}_n$ itself) is then given by $k_n = 2^{i_n}$.

Furthermore, for $i_n \geq 1$, let $S_1, \ldots, S_{k_n}$ denote the sectors arising in this way.[3]

If a particle $\mathbf{P}_n$ intersects the box $\mathbf{B}$, we proceed with the following strategy to determine the intersection arcs $\gamma_{n,k}$ of each sector S_k, see also Fig. 9:

---

[3]Consider the half-spaces

$$V_x^+(x_0) = \{\mathbf{x} = (x, y, z) \in \mathbb{R}^3 : x \geq x_0\} \quad \text{and} \quad V_x^-(x_0) = \{\mathbf{x} = (x, y, z) \in \mathbb{R}^3 : x \leq x_0\},$$

and $V_y^\pm(y_0)$, $V_z^\pm(z_0)$, accordingly. Now consider $V_x^\pm(x_0) \cap V_y^\pm(y_0) = V_{xy}^{\pm\pm}(x_0, y_0)$, and $V_{yz}^{\pm\pm}$, $V_{zx}^{\pm\pm}$, accordingly as well as $V_x^\pm(x_0) \cap V_y^\pm(y_0) \cap V_z^\pm(z_0) = V_{xyz}^{\pm\pm\pm}(x_0, y_0, z_0)$. These are the principal sectors of intersections for the orthogonal planes crossing (x_0, y_0, z_0). For an intersection number $i = 2$ with, for example, the planes B_1 (i.e., $x = x_{\min}$) and B_2 (i.e., $y = y_{\min}$), the sectors are $S_1 = V_{xy}^{++}(x_{\min}, y_{\min})$, $S_2 = V_{xy}^{+-}(x_{\min}, y_{\min})$, $S_3 = V_{xy}^{+-}(x_{\min}, y_{\min})$, $S_4 = V_{xy}^{--}(x_{\min}, y_{\min})$. For $i = 1$ and $i = 3$ the sectors are defined accordingly.

1. Intersect the surface mesh $\mathbf{M}_n$ of $\mathbf{P}_n$ with a coarse, local surface mesh $\mathbf{M}_k$ of the planes $B_i, i = 1, \ldots, i_n$, applying the method described in Section 3.1.2.

2. Get the intersection arcs $\beta_{n,i}$ on the planes $B_i, i = 1, \ldots, i_n$.

3. Consider pairwise intersections of $\beta_{n,i}$, $\beta_{n,j}, i = 1, \ldots, i_n, j = 1, \ldots, i_n, i \neq j$ and determine the common intersection points $\mathbf{v}_{ij} \in \mathbb{R}^3$.

4. Determine the arcs $\gamma_{n,k}$ of each sector $S_k, k = 1, \ldots, 2^{i_n}$ from the plane intersection arcs $\beta_{n,i}, i = 1, \ldots, i_n$.

5. Determine the centroid of $\gamma_{n,k}$.

6. Determine the points $\mathbf{v}_{\text{in}}$ of the initial surface mesh $\mathbf{M} = (\mathbf{v}_n, \mathbf{f}_n)$ which are inside the surface polygon.

7. Project $\mathbf{v}_{\text{in}}$ and $\gamma_{n,k}$ onto the unit sphere and perform a stereographic projection with respect to the centroid.

8. Perform a 2D constrained Delaunay triangulation for the projection (using the method explained in Section 3.1.3), which yields the triangulation $\mathbf{f}_{n,k}$.

9. Consider $(\mathbf{v}_{\text{in}}, \mathbf{f}_{n,k})$ as surface mesh $\mathbf{M}_{n,k}$ of the sector S_k.

10. Performing the above steps for all sectors $k = 1, \ldots, 2^{i_n}$ yields the new closed surface mesh $\mathbf{M}_n = \cup_k \mathbf{M}_{n,k}$ for particle $\mathbf{P}_n$, ensuring the intersection constraints.
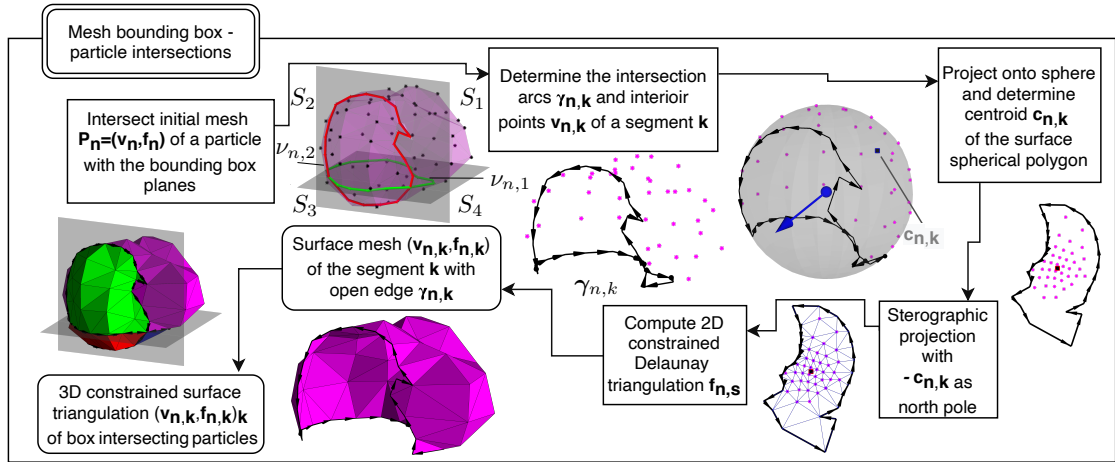

Figure 9: Detailed workflow map of the bounding box-particle intersection.

3.2.3 Meshing of the planes B_i

In order to get a closed surface mesh of $\partial\omega_{\mathbf{E}}$, we need a triangulation of the planes $B_i, i = 1, \ldots, 6$, intersected with all particles. However, we already know the particle-plane intersections, *i.e.*, the arcs $\beta_{n,i}$. However, these arcs have to be intersected with the bounding curve of the rectangle $\bar{B}_i$, yielding the exterior arc α_i of the plane B_i, see Fig. 10. A 2D CDT for the interior mesh-points (u_1^ℓ, u_2^ℓ) of the plane B_i subject to the boundary arcs α_i and $\beta_i = \cup_n \beta_{n,i}$ yields a surface triangulation $\mathbf{M}_i$ for the intersected bounding box plane B_i, and by a repetition of the procedure for all sides $i = 1, \ldots, 6$ a surface mesh $\mathbf{M_B}$ of the intersected box $\mathbf{B}$.

a)
plane-plane arc α_i

particle-plane intersection arcs $\beta_{n,i}$

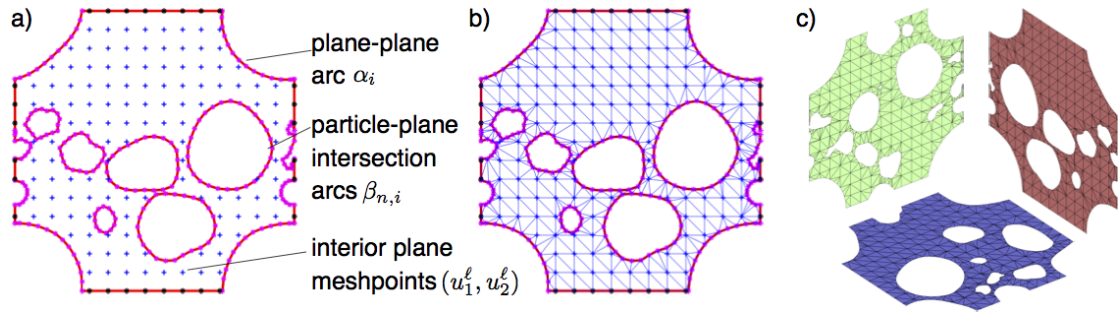interior plane meshpoints (u_1^ℓ, u_2^ℓ)

Figure 10: Detailed workflow map of the bounding box-particle intersection.

3.2.4 Building of a common surface mesh

Based on the surface mesh $\mathbf{M_B}$ of the intersected box $\mathbf{B}$ and the surface meshes $\mathbf{M}_n = \cup_k \mathbf{M}_{n,k}$ of all particles $\mathbf{P}_n$ we can now build a closed surface mesh for $\partial\omega_{\mathbf{E}}$.
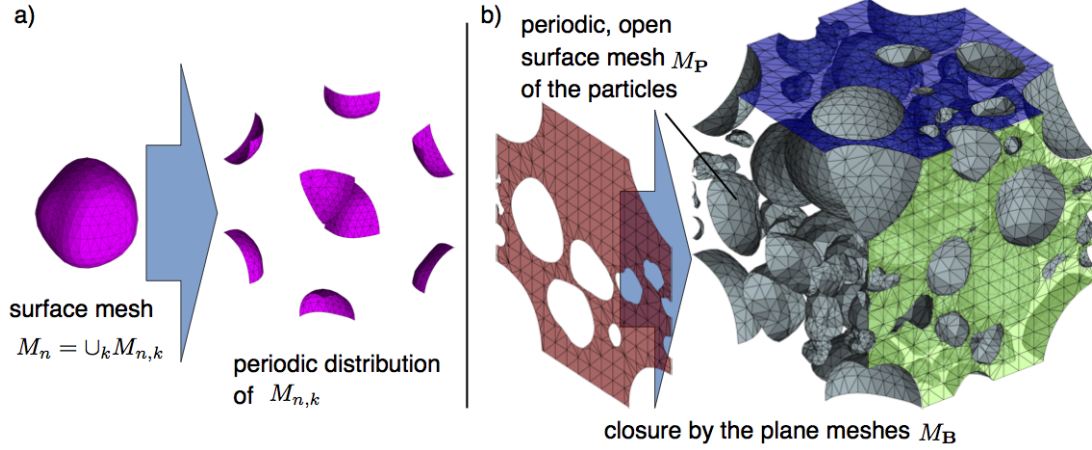
Figure 11: Periodic arrangement of the intersected particle mesh $\mathbf{M}_n = \cup_k \mathbf{M}_{n,k}$ with respect to the periodicity box $\mathbf{B}$ (left). Closure of the open surface mesh $\mathbf{M_P}$ by the open bounding box surface mesh $\mathbf{M_B}$ (right).

The sectorial parts $\mathbf{M}_{n,k}$ are distributed according to the periodicity condition of the bounding box $\mathbf{B}$, denoted by $\hat{\mathbf{M}}_{n,k}$, see Fig. 11a. This yields the periodic open surface mesh $\mathbf{M_P} = \cup_{n=1}^{N} \cup_{k=1}^{2^{i_n}} \hat{\mathbf{M}}_{n,k}$ of all particles. This mesh is now closed by the surface mesh $\mathbf{M_B}$ of the intersected box $\mathbf{B}$, see Fig. 11b, forming a closed surface mesh $\mathbf{M} = \mathbf{M_P} \cup \mathbf{M_B}$ of the microstructure.

3.2.5 Construction of a quality volume mesh

We now have a periodic, closed surface mesh $\mathbf{M} = \mathbf{M_P} \cup \mathbf{M_B}$ of the 3D microstructure. Essentially this is a discrete representation of $\partial \omega_{\mathbf{E}}$. In order to obtain a (discrete) parametrization of $\omega_{\mathbf{E}}$, we rely on a well-established method for 3D constrained Delaunay tetrahedralizations, implemented in TetGen [27, 51]. Note that TetGen is a software package that generates tetrahedral meshes of any 3D polyhedral domain. It generates exact constrained Delaunay tetrahedralizations, boundary conforming Delaunay meshes, and Voronoi partitions. For a closed, intersection free surface mesh $\mathbf{M}$, TetGen generates a high quality volume mesh $\mathbf{M}^V$. Since our surface mesh is perfectly periodic, we force TetGen by flags (`-pqYQA`) to keep the initial surface mesh as boundary, whereby the resulting volume mesh $\mathbf{M}^V$ is also periodic, see the user manual [52] for technical details. In this way, we have a robust method to generate a high quality volume mesh $\mathbf{M}^V$ from a representation $\{(\mathbf{x}_n^0, R_n)\}_{n=1,\dots,N}$ of a periodic microstructure, based on spherical harmonics.
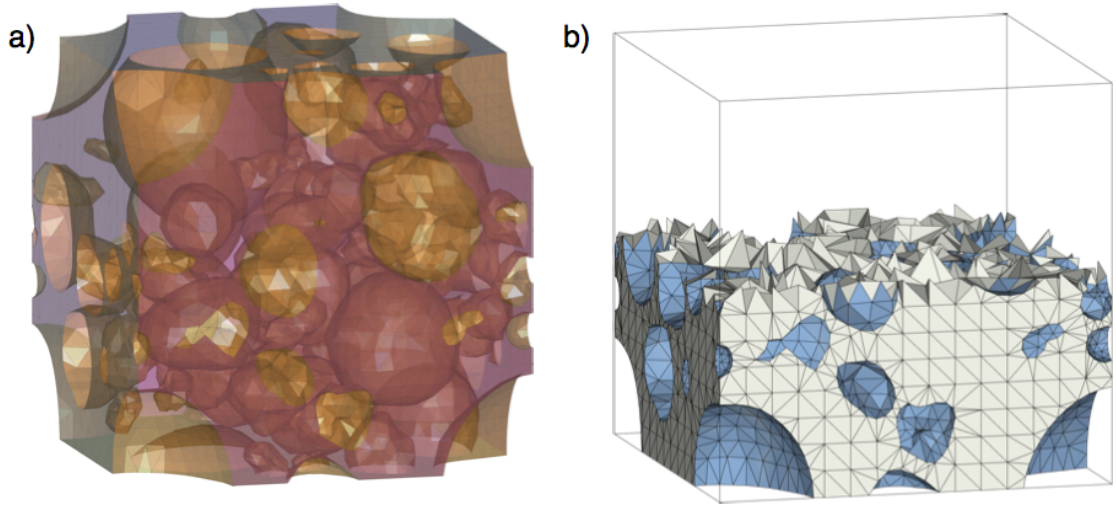
Figure 12: Closed, periodic surface mesh $\mathbf{M}$ of a particulate microstructure represented by spherical harmonics (left). High quality volume mesh $\mathbf{M}^V$ generated with TetGen from the surface mesh $\mathbf{M}$ (right).

4 Numerical results

In this section we discuss three examples of microstructures to provide an impression of the proposed method. The first example considers simple morphologies of equally sized spherical particles, where the porosity is varied and the resulting porous media parameters are compared to the Bruggeman approximation, see Section 4.1. The second example, considered in Section 4.2, deals with a porous microstructure consisting of N particles, where the particle radii are polydisperse. Such microstructures can be found, for example, in porous battery electrodes. The box-size is varied to show some kind of convergence of the porous media parameters, frequently known from stochastic homogenization [53]. The third example ties on this kind of microstructures, where the porosity is varied, see Section 4.3. This is achieved by considering virtually generated microstructures of differently compacted battery electrodes using the stochastic model proposed in [39].

All numerical calculations for the 3D cell problem (CP1) considered in this paper are carried out with COMSOL 5.2 [54] based on the meshes generated by the algorithm explained in Section 3.

4.1 Equally sized spherical particles

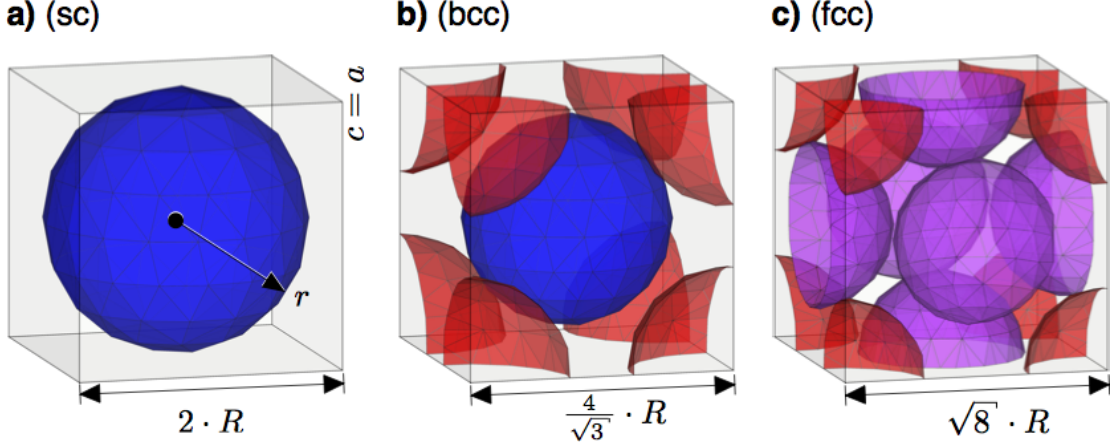**a) (sc)** **b) (bcc)** **c) (fcc)**

Figure 13: Unit cells ω of simple cubic (sc), body centered cubic (bcc), and face centered cubic (fcc) microstructures. The colors encode the number of unit cells shared by a sphere, *i.e.*, blue $= 0$, magenta $= 2$, red $= 4$.

We consider three different Braviais lattices of the cubic crystal system as microstructure. The unit cells ω_{E} are built by simple cubic (sc), body centered cubic (bcc), and face centered cubic (fcc) structures of spheres with some fixed radius $R > 0$, see Fig. 13, where $\omega = [0, b]^3$. We seek to vary the porosity ψ_{E} in this simple example and discuss the porous media parameters $\boldsymbol{\pi}_{\mathrm{E}}$ and $a_{\mathrm{E,S}}$ in terms of ψ_{E}. This can be achieved in two ways, (i) by varying the sphere radius R while keeping the box size b constant, or (ii) by varying the box size b while keeping the radius R constant. Note that these two approaches are, from a materials perspective, completely different. Increasing the box size basically means dispersing the particles in a given volume, while decreasing the particle radius corresponds, e.g., to different synthetization processes leading to smaller particles. For the sake of completeness, we discuss both approaches in parallel, emphasizing, however, that second approach is more realistic.

4.1.1 Variation of the sphere radius, keeping the box size fixed

Consider particles of fixed radius $r \in (0, R)$, where R is some prescribe maximum radius. For a sequence of increasing values $\tilde{r} = \frac{r}{R} \in (0, 1)$ we seek to compute the

effective porous media parameters. The box volume V is given by

$$V = b^3, \qquad \text{where } b = \begin{cases} 2 \cdot R, & \text{for lattice sc,} \\ \frac{4}{\sqrt{3}} \cdot R, & \text{for lattice bcc,} \\ \sqrt{8} \cdot R, & \text{for lattice fcc,} \end{cases}$$

which corresponds to the closest packing when $r = R$. The porosity ψ_{E} of the corresponding material is calculated as

$$\psi_{\mathrm{E}} = \frac{1}{V} \int_{\omega_{\mathrm{E}}} 1 \, dV = \begin{cases} 1 - \frac{\pi}{6}\left(\frac{r}{R}\right)^3 < 1 - 0.5236, & \text{for lattice sc,} \\ 1 - \frac{\sqrt{3}\pi}{8}\left(\frac{r}{R}\right)^3 < 1 - 0.6802, & \text{for lattice bcc,} \\ 1 - \frac{\pi}{3\sqrt{2}}\left(\frac{r}{R}\right)^3 < 1 - 0.7405, & \text{for lattice fcc,} \end{cases}$$

and the interfacial area computes as

$$a_{\mathrm{E,S}} = \frac{1}{V} \int_{\sigma_{\mathrm{E,S}}} 1 \, dA = \begin{cases} \frac{1}{2}\pi \cdot \tilde{r}^2 \frac{1}{R} & < 1.57\frac{1}{R}, & \text{for lattice sc,} \\ \frac{3\sqrt{3}}{8}\pi \cdot \tilde{r}^2 \frac{1}{R} & < 2.04\frac{1}{R}, & \text{for lattice bcc,} \\ \frac{1}{\sqrt{2}}\pi \cdot \tilde{r}^2 \frac{1}{R} & < 2.22\frac{1}{R}, & \text{for lattice fcc.} \end{cases}$$

Note that we can also express the dimensionless radius $\tilde{r}$ in terms of the porosity ψ_{E} which yields the following expressions for the interfacial area:

$$a_{\mathrm{E,S}} = \begin{cases} \frac{1}{2}\pi\left(\frac{6}{\pi}(1-\psi_{\mathrm{E}})\right)^{\frac{2}{3}}\frac{1}{R}, & \text{where } 1-\psi_{\mathrm{E}} \in (0.4764, 1), \text{ for lattice sc,} \\ \frac{3\sqrt{3}}{8}\pi\left(\frac{8}{\sqrt{3}\pi}(1-\psi_{\mathrm{E}})\right)^{\frac{2}{3}}\frac{1}{R}, & \text{where } 1-\psi_{\mathrm{E}} \in (0.3198, 1), \text{ for lattice bcc,} \\ \frac{\pi}{\sqrt{2}}\pi\left(\frac{3\sqrt{2}}{\pi}(1-\psi_{\mathrm{E}})\right)^{\frac{2}{3}}\frac{1}{R}, & \text{where } 1-\psi_{\mathrm{E}} \in (0.2595, 1), \text{ for lattice fcc.} \end{cases}$$

We can now define the interfacial area factor $\theta_{\mathrm{E,S}} = a_{\mathrm{E,S}} \cdot R$ which depends solely on the microstructure, *i.e.*, the type of sphere packing, and on the porosity ψ_{E} via the particle radius r. As expected, the face centered cubic crystal structure (ffc) has a larger interfacial area factor $\theta_{\mathrm{E,S}}$ than the less packed simple cubic structures, see also Fig. 15c.

4.1.2 Variation of the box size, keeping the sphere radius fixed

Next, consider a variation of the box size while keeping the spherical particles at fixed radius R. Note that this corresponds to a dispersion of the particles. The porosity ψ_{E} of the resulting microstructure is calculated as

$$\psi_{\mathrm{E}} = 1 - \frac{N \cdot 4\pi R^3}{3b^3},$$

and the interfacial area as

$$a_{\text{E,S}} = \frac{N 4 \pi R^2}{b^3},$$

where $N = 1$ (sc), $N = 2$ (bcc), and $N = 3$ (fcc). From the two equations given above we get that

$$a_{\text{E,S}} = 3(1 - \psi_{\text{E}}) \tfrac{1}{R}, \tag{5}$$

which is independent of the actual microstructure. This seems to be quite surprising, but the different packings are actually encoded in b^3. In Section 4.2 below, where microstructures with polydisperse particle radii R_n are considered, these examples serve as a kind of reference.
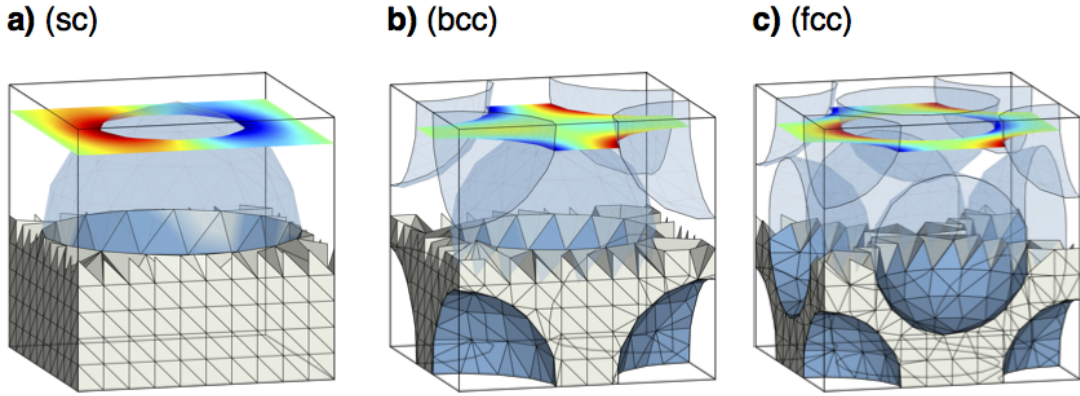
a) (sc)   **b) (bcc)**   **c) (fcc)**

Figure 14: Volume mesh generated by the algorithm presented in Section 3 (lower parts). Numerical solution of $\chi_{\text{E}}^1(y_1, y_2, y_3)\big|_{y_3=0.9}$ (upper parts).

4.1.3 Diffusion corrector and tortuosity

For the sequence of increasing $\tilde{r}$-values considered in Section 4.1.1, we generate 3D meshes of the periodic unit cells ω (meshdata available online) with the algorithm explained in Section 3 and solve the cell problem CP1 numerically, $i.e.$, we determine $\vec{\chi}_{\text{E}}$. The corresponding volume meshes as well as a slice of a numerical solution of $\chi_{\text{E}}^1(y_1, y_2, y_3)\big|_{y_3=0.9}$ are shown in Fig. 14, where the diffusion corrector $\boldsymbol{\pi}_{\text{E}}$ is computed $a\ posteriori$ from Eq. (2). Note that from the definition of $\boldsymbol{\pi}_{\text{E}}$, $i.e.$,

$$\boldsymbol{\pi}_{\text{E}} = \left(1 - \frac{1}{\text{vol}(\omega_{\text{E}})} \int_{\omega_{\text{E}}} \boldsymbol{\nabla} \vec{\chi}_{\text{E}} \, dV\right)$$

25

it follows that $\boldsymbol{\pi}_{\mathrm{E}}$ is actually independent of the particular choice of the approaches (i) or (ii). For all three examples of microstructures consider in Section 4, the diffusion corrector $\boldsymbol{\pi}_{\mathrm{E}}$ essentially reduces to a scalar, *i.e.*, $\boldsymbol{\pi}_{\mathrm{E}} = \pi_{\mathrm{E}}\mathbf{I}$, where $\mathbf{Id}$ denotes the identity matrix. In Fig. 15a, results of the numerical computation of π_{E} with respect to the porosity ψ_{E} are visualized.

Note that, quite commonly, the (scalar) tortuosity corrector τ_{E} is introduced via the effective diffusion coefficient D_u^{eff} of the underlying porous medium. For this, the homogenized transport equation (1) for a simple diffusion flux $\mathbf{J}_u = D_u \nabla u$ is considered, *i.e.*,

$$\psi_{\mathrm{E}} \frac{\partial u}{\partial t} = \mathrm{div}_{\mathbf{x}} \big(\underbrace{\psi_{\mathrm{E}} \boldsymbol{\pi}_{\mathrm{E}} \cdot D_u}_{=D_u^{\mathrm{eff}}} \nabla u \big) + a_{\mathrm{E,S}} \underset{s}{r_u} \,.$$

Newman, Wood and others introduce τ_{E} (implicitly) via $D_u^{\mathrm{eff}} = \frac{\psi_{\mathrm{E}}}{\tau_{\mathrm{E}}} D_u$, which simply yields in our notation $\tau_{\mathrm{E}} = (\pi_{\mathrm{E}})^{-1}$ [55, 56, 57, 58]. Estimation of τ_{E} in terms of the porosity ψ_{E} is performed via the Bruggeman approach [59], claiming that $\tau_{\mathrm{E}} = \psi_{\mathrm{E}}^{-\alpha}$, where α is a microstructure-specific constant. It has been computed as non-linear least squares fit for the lattices sc, bcc and fcc, yielding

$$\alpha^{(\mathrm{sc})} = 0.4111 \,, \quad \alpha^{(\mathrm{bcc})} = 0.3500 \,, \quad \alpha^{(\mathrm{fcc})} = 0.3410 \,.$$

Fig. 15b displays the results of the numerical computation of τ_{E} and, in dashed line, the Bruggeman fit. For microstructures of cubic crystal structures the Bruggeman approximation is, apparently, qualitatively and quantitatively acceptable. However, a major drawback is the underlying assumption of equally sized particles, which is not the case for realistic microstructures. The particle radii within the representative volume element are rather polydispersely distributed, allowing for more dense packing structures and thus smaller values of ψ_{E}. But the simple cubic crystal structures, as well as their Bruggeman approximations, can be considered as a benchmark for the discussion of realistic microstructures.
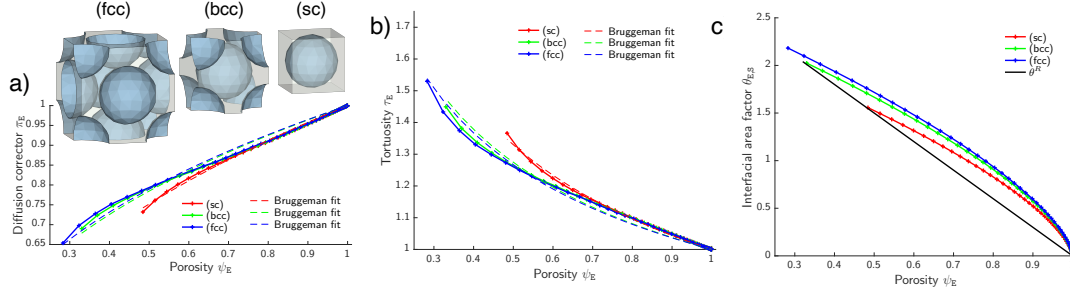
Figure 15: Porous media parameters based on the cell problem CP1: diffusion corrector π_{E} (a), tortuosity $\tau_{\mathrm{E}} = (\pi_{\mathrm{E}})^{-1}$, together with Bruggeman fit $\pi_{\mathrm{E}} = \psi_{\mathrm{E}}^{\alpha}$ (b), and dimensionless interfacial area factor $\theta_{\mathrm{E,S}}$ (c).

4.2 Varying the number of particles

The examples considered in this section deal with the influence of the size of the sampling window and, thus, the number of particles on the porous media parameters. To begin with, in Section 4.2, we consider a system of spheres with a given radius distribution. Afterwards, in Section 4.2.2, we consider a system of non-spherical particles represented by spherical harmonics. In both cases, one unit of length corresponds to $0.44\,\mu\mathrm{m}$.

4.2.1 Spherical particles with polydisperse radii

Obviously, the examples discussed in Section 4.1 are rather of theoretical interest than applicable to realistic porous media since a microstructure described by a single fixed radius is not able to describe complex particle systems. Thus, we now consider a system of N non-overlapping spheres, where the radii $R_1, ..., R_N$ follow a certain probability distribution. For this particular case, it obviously holds that

$$\psi_{\mathrm{E}} = 1 - \frac{\frac{4}{3}\pi \sum_{n=1}^{N} R_n^3}{b^3} \quad \text{and} \quad a_{\mathrm{E,S}} = \frac{4\pi \sum_{n=1}^{N} R_n^2}{b^3}.$$

Hence, we can rewrite $a_{\mathrm{E,S}}$ as

$$a_{\mathrm{E,S}} = 3(1 - \psi_{\mathrm{E}}) \frac{\sum_{n=1}^{N} R_n^2}{\sum_{n=1}^{N} R_n^3} = 3(1 - \psi_{\mathrm{E}}) \underbrace{\frac{\bar{R}\sum_{n=1}^{N} R_n^2}{\sum_{n=1}^{N} R_n^3}}_{=\eta} \frac{1}{\bar{R}} = \frac{6(1 - \psi_{\mathrm{E}})}{d_{3,2}}, \tag{6}$$

where $d_{3,2} = 2 \cdot \frac{\sum_{n=1}^{N} R_n^3}{\sum_{n=1}^{N} R_n^2}$ is known as Sauter diameter or surface area weighted mean diameter [60, 61]. Thus, by comparing Eq. (6) with Eq. (5), one can observe

27

that replacing the fixed radius R considered in Section 4.1 by the mean $\bar{R}$ of a certain radius distribution requires us to introduce the factor η, which depends on the radius distribution. If $\eta < 1$, then the interfacial area $a_{\mathrm{E,S}}$ is smaller compared to the microstructure consisting of a single sphere with $\bar{R}$ as radius. From another point of view, one has to exchange the radius R by the Sauter diameter divided by 2, when considering a distribution of particle radii instead of a single fixed radius. To investigate the influence of the number of spheres N and the standard deviation of the underlying radius distribution on the interfacial area, we exemplarily consider particle radii that are distributed according to a shifted and truncated Birnbaum-Saunders-distribution yielding a mean particle radius of $\bar{R} = 7.2$. This particular choice is motivated by the stochastic 3D microstructure model presented in [39], which will be also used in Section 4.2.2 below. More precisely, we draw $N = 10$ and $N = 10000$, respectively, radii from Birnbaum-Saunders distributions with a fixed mean value of $\mu = 7.2$ and variance σ^2, where σ has been varied from 10^{-2} to 10. As expected, if we increase the number of particles, the volatility of η decreases, see Fig. 16. In particular, for $N = 10000$ particles, η decreases with increasing σ. However, for $N = 10$, one can obtain values of $\eta > 1$ implying a larger interfacial area compared to a single spherical particle whose radius is given by the empirical mean of these 10 radii.
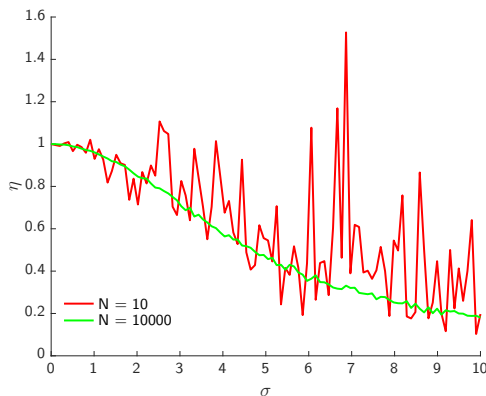

Figure 16: Influence of standard deviation and number of particles on η.

The influence of the particle size distribution on effective tortuosity is beyond the scope of the present paper and will be discussed in a separate (forthcoming) study.

4.2.2 Star-shaped particles represented by spherical harmonics

In this example, we focus on realistic 3D microstructures of a battery electrode consisting of non-spherical particles. For this purpose, we make use of the parametric stochastic microstructure model presented in [39]. For a prescribed cube

28

of side length b, the model yields an analytical expression for the position and radius function of N particles, $i.e.$, $\{(\mathbf{x}_n^0, R_n)\}_{n=1,...,N}$, see Section 2.2. Note that the number of particles N scales approximately with $\mathcal{O}(b^3)$. In particular, the so-called compaction load is fixed to $100\,\text{MPa}$ within this subsection, whereas the influence of varying the compaction load (and thus varying the porosity) is discussed in Section 4.3 below. The distribution of volume-equivalent radii follows the same shifted Birnbaum-Saunders distribution as in the previous example. To investigate the influence of the size of the bounding box on the resulting porous media parameters, ten model realizations have been generated for each box size $b \in \{25, 50, 75, 100, 125, 150, 175, 200\}$ and, subsequently, a periodic volume mesh has been determined by using the methodology described in Section 3. The corresponding surface and volume mesh files are available as supplementary material. Figure 17 shows the histogram as well as the periodic surface mesh generated by a single model realization using the box sizes $b \in \{50, 100, 150, 200\}$.
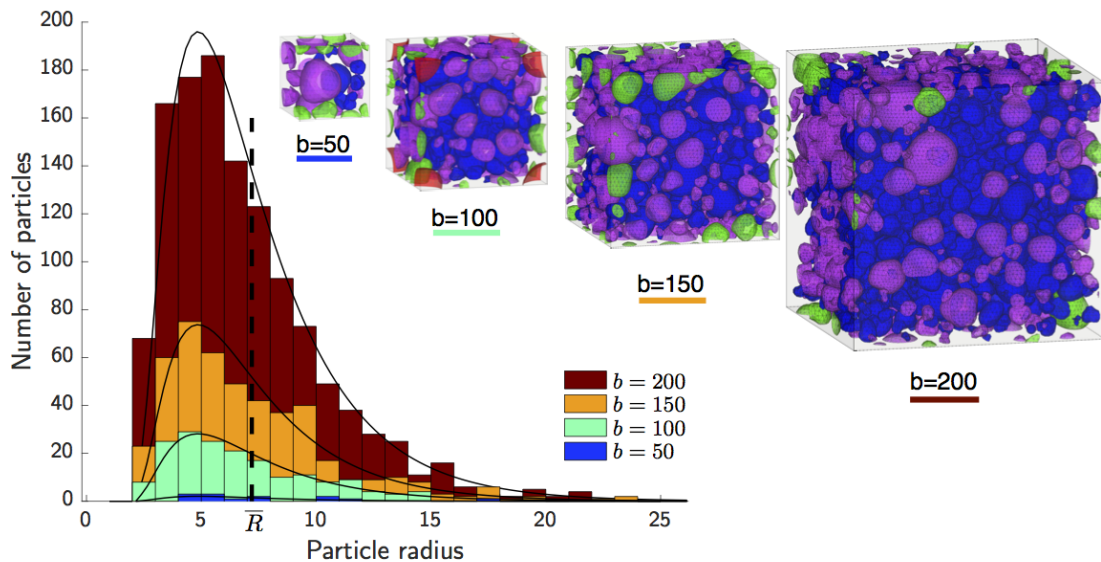

Figure 17: Histogram of the particle radii for an increasing box size and periodic surfaces meshes for box sizes $b \in \{50, 100, 150, 200\}$.

Based on the volume meshes of ten model realizations for each box size b, the porosity ψ_E, interfacial area $a_\text{E,S}$ and (diffusion) corrector $\boldsymbol{\pi}_\text{E}$ have been computed. Fig. 18 shows the results for 10 realizations per box size, where each plus sign corresponds to one realization and the patch is the convex hull of all realizations per box size. As the box size increases, this variation declines and we obtain some kind of convergence of the parameters. This effect is also known in stochastic homogenization, where the parameters of simulated microstructures converge to

29

some effective parameters as the representative volume element increases. Furthermore, one can observe that a box size of at least 75 drastically reduces the variation within the parameters of different model realizations compared to a box size of 25 and 50, respectively. In addition, the Bruggeman relation seems to lead to a slight, systematic overestimation of the diffusion corrector, which in turn leads to a slight underestimation of effective tortuosity.
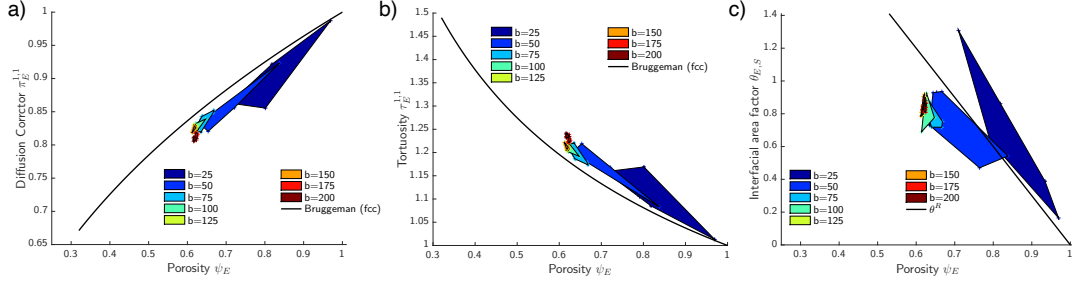

Figure 18: Porous media parameters for various box sizes: diffusion corrector $\pi_{\mathrm{E}}^{1,1}$ (a), tortuosity $\tau_{\mathrm{E}}^{1,1} = (\pi_{\mathrm{E}}^{1,1})^{-1}$ (b) and interfacial area $\theta_{\mathrm{E,S}}$ (c). The patch displays the convex hull of the corresponding values for the 10 realizations and each box size b.

4.3 Star-shaped particles with different degrees of compaction

In this section we consider a series of electrode morphologies, where the degree of compaction and thus the porosity ψ_{E} is varied. In [39], a stochastic model was fitted to tomographic image data of eight differently compacted cathodes. This model has been adopted to the periodic case, see Section 3, and again 10 realizations have been generated for each of the eight different compaction loads $m = 0\,\mathrm{MPa}, 100\,\mathrm{MPa}, \dots, 1000\,\mathrm{MPa}$ with a box size $b = 100$. Note that, as in Section 4.2 one unit of length corresponds to $0.44\,\mu\mathrm{m}$. The mesh files are available online via the supplementary information.

Once again, the porous media parameters have been computed based on the 3D solution of the cell problem CP 1, see Fig. 19. As expected, the diffusion corrector decreases with decreasing porosity ψ_{E} and stays below the Bruggeman (bcc) approximation. In addition, the largest changes with regard to the diffusion corrector as well as tortuosity can be observed for low compaction loads, whereas higher compaction loads have only a minor influence on the porous media parameters. This pattern can also be observed with regard to the 3D microstructure, see [62]. Since the computation of porous media parameters is carried out with ten realizations of the stochastic 3D microstructure per compaction load, we are

also able to gain some insights on the variability of the corresponding effective properties, which is also observed experimentally [63]. It can be observed that different degrees of compaction and thus different porosities can lead to the same interfacial area factor $\theta_{E,S}$. This shows that the porosity alone might not be sufficient to estimate the interfacial area factor, which is crucial for the electrochemical performance. Nevertheless we find, within the variance of the realizations, that the interfacial area factor $\theta_{E,S}$ increases with decreasing porosity ψ_E and the reference interfacial area factor $\theta_{E,S}^R$ of equally sized spheres remains an upper bound for $\theta_{E,S}$. Note further that for a fixed compaction load, this characteristic also shows some variability, which is caused by the stochastic nature of the underlying 3D microstructure model. Our method can thus be considered as versatile tool to investigate the variablility of microstructures, and their corresponding porous media parameters, (i) for a fixed process parameter by considering different realizations and (ii) for a series of 3D microstructures that arise from a manufacturing process with different process parameters.
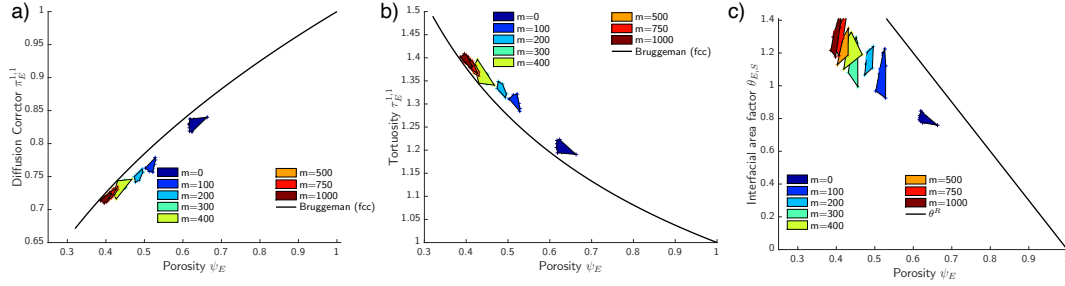

Figure 19: Porous media parameters for various compaction loads: diffusion corrector $\pi_E^{1,1}$ (a), tortuosity $\tau_E^{1,1} = (\pi_E^{1,1})^{-1}$ (b) and interfacial area factor $\theta_{E,S}$ (c). The patch displays the convex hull of the corresponding values for the 10 realizations and each compaction load.

5 Conclusion and outlook

In this paper, we presented a novel, robust method for generating high-quality volume meshes based on the spherical harmonics representation of particulate microstructures. For this purpose, a stochastic 3D microstructure model has been used in order to generate virtual, but realistic two-phase microstructures as structural input for the mesh generation procedure. In addition, the presented method is able to handle periodic boundary conditions in a predefined set of directions as well. After the generation of the volume mesh, partial differential equations can be solved numerically, where the mesh itself can be generated as precise as desired by increasing the number of mesh points since the underlying microstructure is de-

scribed analytically. We applied the proposed method exemplarily to cathodes in lithium-ion batteries which have been manufactured for eight different compaction loads. However, due to its generality, our approach is applicable to a broad range of functional materials for which effective properties are of interest. In general, the combination of numerically solving physically-motivated partial differential equations using volume meshes and stochastic 3D microstructure modeling allows to systematically investigate the impact of the materials' morphology on the resulting performance. This approach, called virtual materials testing, can be used to facilitate the design of functional materials with optimized effective properties just at the cost of computer simulations. In particular, in a forthcoming study, we plan to systematically quantify the influence of microstructural characteristics such as volume fraction, specific surface area and constrictivity on porous media parameters via an extensive simulation study with several thousands virtually generated battery electrodes.

Acknowledgment

References

[1] W. R. Gardner, "Solutions of the flow equation for the drying of soils and other porous media," *Soil Science Society of America Journal*, vol. 23, no. 3, p. 183–187, 1959.

[2] Y. Mualem, "A new model for predicting the hydraulic conductivity of unsaturated porous media," *Water Resources Research*, vol. 12, no. 3, p. 513–522, 1976.

[3] M. Hain and P. Wriggers, "Numerical homogenization of hardened cement paste," *Computational Mechanics*, vol. 42, no. 2, p. 197–212, 2008.

[4] F. Bouchelaghem, A. Benhamida, and H. Dumontet, "Mechanical damage behaviour of an injected sand by periodic homogenization method," *Computational Materials Science*, vol. 38, no. 3, p. 473–481, 2007.

[5] A. Gully, H. Liu, S. Srinivasan, A. K. Sethurajan, S. Schougaard, and B. Protas, "Effective transport properties of porous electrochemical materials – a homogenization approach," *Journal of The Electrochemical Society*, vol. 161, no. 8, p. E3066–E3077, 2014.

[6] F. Ciucci and W. Lai, "Derivation of micro/macro lithium battery models from homogenization," *Transport in Porous Media*, vol. 88, no. 2, p. 249–270, 2011.

[7] M. Ender, "An extended homogenized porous electrode model for lithium-ion cell electrodes," *Journal of Power Sources*, vol. 282, p. 572–580, 2015.

[8] B. Khuzhayorov, J.-L. Auriault, and P. Royer, "Derivation of macroscopic filtration law for transient linear viscoelastic fluid flow in porous media," *International Journal of Engineering Science*, vol. 38, no. 5, p. 487–504, 2000.

[9] S. Torquato, *Random Heterogeneous Materials: Microstructure and Macroscopic Properties.* Springer, 2013.

[10] S. Cho, C.-F. Chen, and P. P. Mukherjee, "Influence of microstructure on impedance response in intercalation electrodes," *Journal of The Electrochemical Society*, vol. 162, no. 7, p. A1202–A1214, 2015.

[11] Y. Shin and A. Manthiram, "Influence of microstructure on the electrochemical performance of $LiMn_{2-y-z}Li_yNi_zO_4$ spinel cathodes in rechargeable lithium batteries," *Journal of Power Sources*, vol. 126, no. 1, p. 169–174, 2004.

[12] T. Waldmann, M. Wilka, M. Kasper, M. Fleischhammer, and M. Wohlfahrt-Mehrens, "Temperature dependent ageing mechanisms in lithium-ion batteries - a post-mortem study," *Journal of Power Sources*, vol. 262, p. 129–135, 2014.

[13] W. Li and J. C. Currie, "Morphology effects on the electrochemical performance of $LiNi_{1-x}Co_xO_2$," *Journal of The Electrochemical Society*, vol. 144, no. 8, p. 2773–2779, 1997.

[14] J. Habedank, L. Kraft, A. Rheinfeld, C. Krezdorn, A. Jossen, and M. Zaeh, "Increasing the discharge rate capability of lithium-ion cells with laser-structured graphite anodes: Modeling and simulation," *Journal of The Electrochemical Society*, vol. 165, p. A1563–A1573, 2018.

[15] P. Smyrek, J. Pröll, H. Seifert, and W. Pfleging, "Laser-induced breakdown spectroscopy of laser-structured li(nimncoo)₂ electrodes for lithium-ion batteries," *Journal of The Electrochemical Society*, vol. 163, p. A19–A26, 2016.

[16] L. S. Kremer, A. Hoffmann, T. Danner, S. Hein, B. Prifling, D. Westhoff, C. Dreer, A. Latz, V. Schmidt, and M. Wohlfahrt-Mehrens, "Manufacturing process for improved ultra-thick cathodes in high-energy lithium-ion batteries," *Energy Technology*, vol. 8, no. 2, p. 1900167, 2020.

[17] G. Allaire, "Homogenization and two-scale convergence," *SIAM Journal on Mathematical Analysis*, vol. 23, no. 6, p. 1482–1518, 1992.

[18] D. Cioranescu, A. Damlamian, P. Donato, G. Griso, and R. Zaki, "The periodic unfolding method in domains with holes," *SIAM Journal on Mathematical Analysis*, vol. 44, no. 2, p. 718–760, 2012.

[19] B. Amaziane and L. Pankratov, "Homogenization of a reaction-diffusion equation with robin interface conditions," *Applied Mathematics Letters*, vol. 19, no. 11, p. 1175 – 1179, 2006.

[20] G. Allaire, "Homogenization of the Stokes flow in a connected porous medium," *Asymptotic Analysis*, vol. 2, no. 3, p. 203–222, 1989.

[21] D. Westhoff, I. Manke, and V. Schmidt, "Generation of virtual lithium-ion battery electrode microstructures based on spatial stochastic modeling," *Computational Materials Science*, vol. 151, p. 53–64, 2018.

[22] A. Akpoyomare, M. Okereke, and M. Bingley, "Virtual testing of composites: Imposing periodic boundary conditions on general finite element meshes," *Composite Structures*, vol. 160, p. 983–994, 2017.

[23] F. Reis and F. Andrade Pires, "A mortar based approach for the enforcement of periodic boundary conditions on arbitrarily generated meshes," *Computer Methods in Applied Mechanics and Engineering*, vol. 274, p. 168–191, 2014.

[24] K. Schneider, B. Klusemann, and S. Bargmann, "Automatic three-dimensional geometry and mesh generation of periodic representative volume elements for matrix-inclusion composites," *Advances in Engineering Software*, vol. 99, p. 177–188, 2016.

[25] C. Dobrzynski, M. Melchior, L. Delannay, and J.-F. Remacle, "A mesh adaptation procedure for periodic domains," *International Journal for Numerical Methods in Engineering*, vol. 86, no. 12, p. 1396–1412, 2011.

[26] F. Fritzen and T. Böhlke, "Periodic three-dimensional mesh generation for particle reinforced composites with application to metal matrix composites," *International Journal of Solids and Structures*, vol. 48, no. 5, p. 706 – 718, 2011.

[27] H. Si, "TetGen, a Delaunay-based quality tetrahedral mesh generator," *ACM Transactions on Mathematical Software*, vol. 41, no. 2, 2015.

[28] A. Bezrukov, M. Bargieł, and D. Stoyan, "Statistical analysis of simulated random packings of spheres," *Particle & Particle Systems Characterization*, vol. 19, no. 2, p. 111–118, 2002.

[29] J. Mosćiński, M. Bargieł, Z. Rycerz, and P. Jakobs, "The force-biased algorithm for the irregular close packing of equal hard spheres," *Molecular Simulation*, vol. 3, p. 201–212, 1989.

[30] G. B. Arfken and H. J. Weber, *Mathematical Methods for Physicists*. Elsevier / Academic Press, 6 ed., 2005.

[31] D. A. Varshalovich, A. N. Moskalev, and V. K. Khersonskii, *Quantum Theory of Angular Momentum*. Singapore: World Scientific, 1988.

[32] M. Modest, *Radiative Heat Transfer*. Oxford: Elsevier Science, 3 ed., 2013.

[33] K. Atkinson and W. Han, *Spherical Harmonics and Approximations on the Unit Sphere: An Introduction*. Lecture Notes in Mathematics, Berlin: Springer, 2012.

[34] E. U. Condon and G. H. Shortley, *The Theory of Atomic Spectra*. Cambridge University Press, 1935.

[35] J. Feinauer, A. Spettl, I. Manke, S. Strege, A. Kwade, A. Pott, and V. Schmidt, "Structural characterization of particle systems using spherical harmonics," *Materials Characterization*, vol. 106, p. 123–133, 2015.

[36] D. Marinucci and G. Peccati, *Random Fields on the Sphere: Representation, Limit Theorems and Cosmological Applications*. London Mathematical Society Lecture Note Series, Cambridge University Press, 2011.

[37] A. Lang and C. Schwab, "Isotropic Gaussian random fields on the sphere: Regularity, fast simulation and stochastic partial differential equations," *The Annals of Applied Probability*, vol. 25, no. 6, p. 3047–3094, 2015.

[38] J. Feinauer, T. Brereton, A. Spettl, M. Weber, I. Manke, and V. Schmidt, "Stochastic 3D modeling of the microstructure of lithium-ion battery anodes via Gaussian random fields on the sphere," *Computational Materials Science*, vol. 109, p. 137–146, 2015.

[39] B. Prifling, D. Westhoff, D. Schmidt, H. Markötter, I. Manke, V. Knoblauch, and V. Schmidt, "Parametric microstructure modeling of compressed cathode materials for Li-ion batteries," *Computational Materials Science*, vol. 169, p. 109083, 2019.

[40] Q. Fang and D. A. Boas, "Tetrahedral mesh generation from volumetric binary and grayscale images," in *2009 IEEE International Symposium on Biomedical Imaging: From Nano to Macro*, p. 1142–1145, 2009.

[41] M. Wenninger, *Spherical Models.* Dover, 1999.

[42] M. Deserno, "How to generate equidistributed points on the surface of a sphere." `https://www.cmu.edu/biolphys/deserno/pdf/sphere_equi.pdf`, 2004.

[43] C. B. Barber, D. P. Dobkin, and H. Huhdanpaa, "The quickhull algorithm for convex hulls," *ACM Transactions on Mathematical Software*, vol. 22, no. 4, p. 469–483, 1996.

[44] MATLAB, *Version 9.4.0.813654 (R2018a).* Natick, Massachusetts: The MathWorks Inc., 2018.

[45] T. Möller, "A fast triangle-triangle intersection test," *Journal of Graphics Tools*, vol. 2, no. 2, p. 25–30, 1997.

[46] J. Tuszynski, "Surface intersection," tech. rep., MATLAB Central File Exchange, https://www.mathworks.com/matlabcentral/fileexchange/48613-surface-intersection, 2020.

[47] O. Devillers and P. Guigue, "Faster triangle-triangle intersection tests," *INRIA*, vol. RR-4488, 2002.

[48] L. P. Chew, "Constrained Delaunay triangulations," in *Proceedings of the Third Annual Symposium on Computational Geometry*, SCG '87, p. 215–222, Association for Computing Machinery, 1987.

[49] J. R. Shewchuk, "General-dimensional constrained Delaunay and constrained regular triangulations, I: Combinatorial properties," *Discrete & Computational Geometry*, vol. 39, no. 1, p. 580–637, 2008.

[50] J. E. Brock, "The inertia tensor for a spherical triangle," *Journal of Applied Mechanics*, vol. 42, no. 1, p. 239–239, 1975.

[51] H. Si, "WIAS software TetGen - A quality tetrahedral mesh generator and a 3D Delaunay triangulator." Available online: `http://wias-berlin.de/software/index.jsp?id=TetGen`.

[52] H. Si, *TetGen: A Quality Tetrahedral Mesh Generator and 3D Delaunay Triangulator.* User's Manual, Version 1.5, Weierstrass Institute for Applied Analysis and Stochastics, Berlin, 2013.

[53] J. Fischer and S. Neukamm, "Optimal homogenization rates in stochastic homogenization of nonlinear uniformly elliptic equations and systems," *arXiv*, no. 1908.02273, 2019.

[54] "COMSOL Multiphysics® Version 5.2." `www.comsol.com`. COMSOL AB.

[55] D.-W. Chung, M. Ebner, D. R. Ely, V. Wood, and R. E. García, "Validity of the Bruggeman relation for porous electrodes," *Modelling and Simulation in Materials Science and Engineering*, vol. 21, no. 7, p. 074009, 2013.

[56] B. Tjaden, S. J. Cooper, D. J. Brett, D. Kramer, and P. R. Shearing, "On the origin and application of the Bruggeman correlation for analysing transport phenomena in electrochemical systems," *Current Opinion in Chemical Engineering*, vol. 12, p. 44 – 51, 2016. Nanotechnology / Separation Engineering.

[57] J. Newman, K. Thomas, *Electrochemical Systems*. J. Wiley & Sons, 2014.

[58] M. Ebner and V. Wood, "Tool for tortuosity estimation in lithium ion battery porous electrodes," *Journal of The Electrochemical Society*, vol. 162, no. 2, p. A3064–A3070, 2014.

[59] D. A. G. Bruggeman, "Berechnung verschiedener physikalischer Konstanten von heterogenen Substanzen. I. Dielektrizitätskonstanten und Leitfähigkeiten der Mischkörper aus isotropen Substanzen," *Annalen der Physik*, vol. 416, no. 7, p. 636–664, 1935.

[60] H. Merkus, *Particle Size Measurements: Fundamentals, Practice, Quality*. Springer, 2009.

[61] T. Allen, *Powder Sampling and Particle Size Determination*. Elsevier, 2003.

[62] K. Kuchler, B. Prifling, D. Schmidt, H. Markötter, I. Manke, T. Bernthaler, V. Knoblauch, and V. Schmidt, "Analysis of the 3D microstructure of experimental cathode films for lithium-ion batteries under increasing compaction," *Journal of Microscopy*, vol. 272, no. 2, p. 96–110, 2018.

[63] S. J. Harris and P. Lu, "Effects of inhomogeneities - nanoscale to mesoscale - on the durability of Li-ion batteries," *The Journal of Physical Chemistry C*, vol. 117, no. 13, p. 6481–6492, 2013.